Flexible and Printed Electronics

TOPICAL REVIEW • OPEN ACCESS

Additively fabricated on-skin sensors for mechanical and thermal biosignal monitoring

To cite this article: Mika-Matti Laurila 2023 *Flex. Print. Electron.* **8** 033002

View the article online for updates and enhancements.

You may also like

- Deep learning for biosignal control: insights from basic to real-time methods with recommendations
Arnau Dillen, Denis Steckelmacher, Kyriakos Efthymiadis et al.
- Analysis of CBCT-based image guidance for a large cohort of lung cancer patients treated with SABR
Essa Mayyas, Ning Wen, Carri Glide-Hurst et al.
- Review—Recent Progress in the Diversity of Inkjet-Printed Flexible Sensor Structures in Biomedical Engineering Applications
Hanim Hussin, Norhayati Soin, Sharifah Fatmadiana Wan Muhamad Hatta et al.

This content was downloaded from IP address 130.230.26.20 on 05/09/2023 at 06:49

Flexible and Printed Electronics

TOPICAL REVIEW

Additively fabricated on-skin sensors for mechanical and thermal biosignal monitoring

Mika-Matti Laurila

Department of Electrical Engineering, Tampere University, Tampere, Finland

E-mail: mika-matti.laurila@tuni.fi

Keywords: biosignal measurement, additive fabrication technologies, printed electronics, epidermal electronics, wearable electronics, healthcare monitoring, electronic tattoo (e-tattoo) sensors

OPEN ACCESS

RECEIVED
30 March 2023

REVISED
25 April 2023

ACCEPTED FOR PUBLICATION
8 June 2023

PUBLISHED
3 August 2023

Original content from this work may be used under the terms of the Creative Commons Attribution 4.0 licence.

Any further distribution of this work must maintain attribution to the author(s) and the title of the work, journal citation and DOI.

Abstract

Continuous biosignal monitoring with on-skin worn sensor devices enables out-of-hospital patient monitoring (i.e. ubiquitous healthcare), which has high potential to reduce various disease-related societal costs through large-scale screening of disease risk groups. However, novel fabrication methods need to be adopted to enable the required large-scale deployment of such devices. Additive fabrication technologies have emerged as potential candidates to meet this challenge due to their low material consumption, scalability, and compatibility with skin-conformable low T_g polymeric substrates. This review article discusses recent advances in additively fabricated on-skin biosignal sensors and focuses on the following topics: (1) available additive fabrication technologies; (2) on-skin measurable mechanical and thermal biosignals and related additively fabricated biosignal sensors; and (3) the emerging field of printed electronic tattoo (e-tattoo)-type mechanical and thermal biosignal sensors.

1. Introduction

Additive fabrication technologies in electronics are characterized by the use of solution processable, electrically functional materials, and their selective, layer-by-layer deposition to form electronic devices [1]. In contrast to lithographic fabrication processes, additive fabrication promises lower tooling costs, fewer process steps, and less material consumption, thereby enabling, for example, higher levels of batch-to-batch customization, more affordable fabrication of large-area devices, and reduced environmental impact [1–3]. The use of low processing temperature materials, such as conductive metal nanoparticle inks (for electrodes), semiconductive polymer inks (for transistors), and piezoelectric polymer inks (for electroactive layers of sensors), further enables the use of comparably cheap low glass transition temperature (T_g) polymeric substrates [1, 2]. The use of polymeric substrates, in turn, enables new functionalities such as stretchability and softness [4–13], which are unattainable with rigid, silicon-based substrates conventionally used in electronics fabrication.

Recently, it has been proposed that these novel functionalities be used in the field of on-skin biosignal monitoring, where the mechanical properties of electronic devices need to match the mechanical properties of the skin [6–50]. On-skin biosignal monitoring with affordable and highly skin-conformable biosignal monitoring systems could enable continuous at-home monitoring of patients before and after medical treatment. Similarly, it could enable cost-effective screening of chronic, life threatening diseases on a scale that cannot be achieved with current methods, which require hospital visits, the use of expensive/bulky equipment, and the presence of medical professionals [17]. This, in turn, could lead to significant societal benefits through reduced mortality and healthcare costs.

Based on the above considerations, a topical review of the available additive fabrication technologies and additively fabricated on-skin biosignal sensors is highly needed to: (1) provide a comprehensive overview of the current state of the technology available; (2) identify potential shortcomings and/or overlooked aspects in the field;

© 2023 The Author(s). Published by IOP Publishing Ltd

(3) identify promising areas for future development; and (4) promote the use of additive fabrication methods for on-skin biosignal sensors. This review focuses on mechanical and thermal biosignal sensors as these have synergies regarding the used materials and sensor designs; as an example, capacitive sensors can be implemented for both pressure *and* temperature sensing, assuming suitable material properties of the dielectric (i.e. a suitable Young's modulus and thermal coefficient of expansion). Similarly, a piezoelectric sensor can be used for both mechanical deformation and temperature sensing if it also has pyroelectric properties (e.g. poly(vinylidenefluoride-trifluoroethylene) (P(VDF-TrFE))).

The article is arranged as follows. Section 2 introduces the various additive fabrication technologies that can be used in on-skin biosignal sensor fabrication. It concludes with a comparison table of technology capabilities (e.g. throughput, resolution, material compatibilities, etc). In section 3, the measured physical properties (e.g. mechanical deformation) are discussed on a general level and are related to potential biosignals, which can be measured using the said physical properties (e.g. arterial pulse waves). This is followed by a more detailed explanation of the material properties (e.g. piezoelectricity) that can be utilized to measure the said physical properties/biosignals. This section also includes examples of recent additively fabricated on-skin sensors utilizing the specific material properties. A comparison table is included at the end of each section. Section 4 briefly discusses the emerging field of additively fabricated electronic tattoo (e-tattoo) type biosignal sensors. Section 5 summarizes the state-of-the-art technology and discusses future development possibilities in the field of on-skin biosignal monitoring.

2. Additive fabrication technologies

Additive fabrication technologies can be categorized into digital and nondigital technologies based on whether the printing device uses a digital print file or a physical mask to create the desired pattern. It is also possible to categorize them based on process-related parameters such as resolution, throughput, ability to produce two-dimensional (2D) vs. three-dimensional (3D) structures, or whether the print plate or roll comes into contact with the substrate or not (i.e. contact vs. contactless printing methods). Yet another way to categorize the printing methods is to divide them based on their original intended purpose into conventional printing tools, which were originally used in graphic art (even as early as the 17th century), and novel printing tools, which have been developed specifically for additive fabrication. However, this review follows an approach where they are divided into contact-printing methods (e.g. inkjet, screen, and roll-to-roll printing methods) and novel printing methods (e.g. electrohydrodynamic inkjet, aerosol jet, nanoimprint lithography, 3D printing). A comparison table (table 1) is included at the end of this section to illustrate the differences between various technologies.

2.1. Conventional printing methods

2.1.1. Inkjet printing

Inkjet printing was originally developed in the 1970s for the printing of office documents from computer-generated digital print files. Similar to these early devices, modern inkjet printers adapted to printed electronics are of the drop-on-demand type; that is, the position of each deposited droplet on the substrate can be controlled 'on demand'. This drop-on-demand nature of the printer allows for rapid batch-to-batch manipulation of the dimensions of the printed pattern and makes inkjet printing especially suitable for rapid prototyping. However, it does not exclude high throughput as this can be increased simply by increasing the number of nozzles in the printhead (e.g. 2041 nozzle Samba GL [1]), and by integrating the printhead into a roll-to-roll type device. The resulting throughput can be comparable to flexographic roll-to-roll printing ($\sim$500 m min^{-1}) [2]. Furthermore, the noncontact nature of inkjet printing makes it insensitive to the mechanical properties of the substrate, thereby enabling printing onto delicate and fragile substrates. This is in clear contrast to, for example, roll-to-roll methods, which are limited to flexible substrates [3, 51].

Most inkjet printers employed for electronics fabrication are of the piezoelectric type; that is, the droplet generation is based on piezoelectrically actuated pressure waves, which drive the droplet out of the nozzle (see figure 1(A)). From the printer side, print quality can be controlled by varying the driving voltage parameters (e.g. peak voltage, pulse width, slope) of the piezoelectric element and the resolution of the printed pattern. Regarding the latter, the extent of overlap of the neighboring droplets results in different line morphologies, and this parameter needs to be carefully optimized to achieve uniform lines [52] (see figure 1(B)). The maximum resolution (i.e. line width) on substrates with optimized wetting conditions is in the order of 20–50 μm, which is average when compared to other printing technologies. However, the droplet positioning accuracy (i.e. the minimum spacing between two parallel lines) can be in the order of 10 μm, which is somewhat smaller than the average achievable with other printing technologies [2, 53].

The challenges of inkjet printing are mainly related to ink formulation because the ink viscosity and surface tension range are limited by the demands of the printhead (e.g. small nozzle diameter, high pressure/shear forces during ejection). These

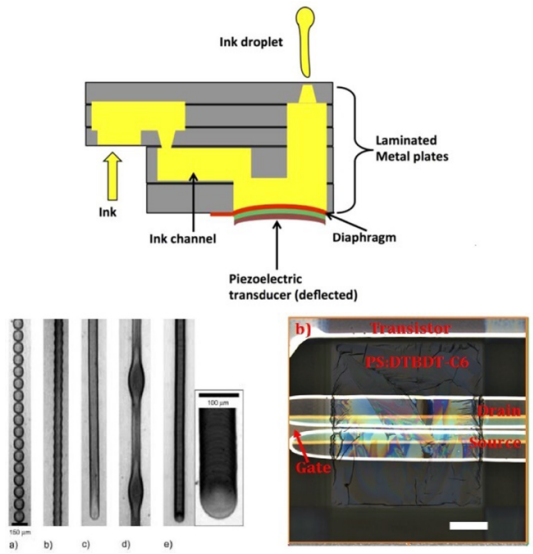

Figure 1. (A) The functioning principle of a piezoelectric inkjet printer. Reproduced from [54]. Copyright The Author(s). CC BY 4.0. (b) The effect of drop spacing on inkjet-printed line morphologies. Reprinted with permission from [52]. Copyright (2008) American Chemical Society. (C) Transistor with inkjet-printed source and drain electrodes; channel length is approximately 10 μm. Reproduced from [53]. CC BY 3.0.

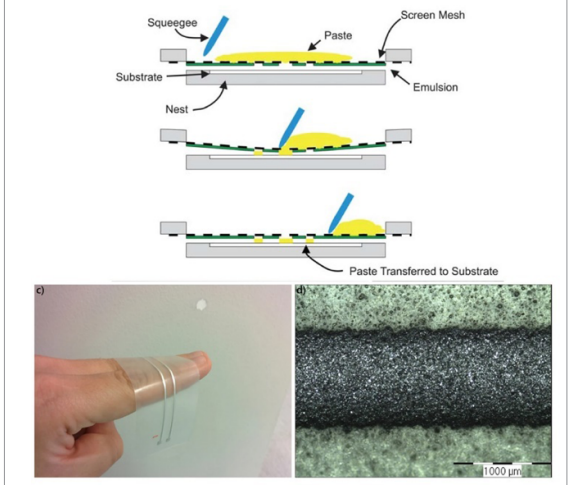

Figure 2. (A) Functioning principle of a screen printer. Reproduced from [60] with permission from the Royal Society of Chemistry. (B) Screen-printed stretchable Ag-flake electrodes on a thermoplastic polyurethane substrate. Reproduced from [4]. CC BY 4.0.

demands also set limits, for example, for the boiling point of suitable solvents, particle dispersion, and solid content of the particulate inks to enable stable jetting performance and high device yields [3, 51].

Regarding on-skin biosignal sensors, inkjet printing shows great potential due to its ability to form very thin films (i.e. single layer thickness of a few hundred nanometers [55]). This is especially important for the fabrication of sensors and circuits that aim to maximize unobtrusiveness and skin-conformability by minimizing the device thickness (i.e. so-called ultrathin devices) [53, 56]. The high droplet positioning accuracy of inkjet printers can be used, for example, for additive fabrication of small channel length (order of 10 μm) transistors for biosignal amplifiers [53] (see figure 1(C)) and for the fabrication of high-uniformity interdigitated charge collectors for piezoelectric biosignal sensors [57].

2.1.2. Screen printing

Unlike inkjet printing technology, which was adopted for printing electronics fabrication only relatively recently, screen printing has been used in electronics fabrication for a longer time and can therefore be considered a relatively mature technology. There are two types of screen printer setups: a rotary screen (e.g. roll-to-roll type) and a flatbed screen (e.g. sheet-to-sheet type; see figure 2(A)). The basic components in both cases are the same: a screen consisting of a fine wire mesh that is exposed in the area of the pattern to be printed, and a squeegee to spread the ink onto the screen and to drive it through the exposed mesh onto the substrate. In the case of a rotary screen, the squeegee and ink are positioned inside the rotary screen, and an impression cylinder is used to apply pressure between the substrate and the rotary screen to transfer the pattern. In a flatbed screen, the screen is strained on a planar frame, and the squeegee is used to apply pressure on the substrate and drive the ink through the screen onto the substrate placed underneath it. In the latter case, the print quality is controlled by adjusting the snap-off distance (i.e. the distance between the screen and substrate when the squeegee is not pressed against the screen) and the squeegee pressure/speed/angle [58, 59].

Compared to , for example, inkjet printing, screen printing is more robust regarding the ink formulation and allows for printing of high viscosity, high solid content inks with a larger particle size (e.g. micrometer-long Ag-nanowires [5] and -flakes [4]). Regarding on-skin biosignal sensors, this feature is especially interesting because it enables the use of stretchable nanocomposite inks to make full use of the potential of low T_g elastomeric substrates for the fabrication of stretchable devices that better match the mechanical properties of the skin [4] (see figure 2(B)). Furthermore, by employing the rotary screen, the fabrication throughput can be increased significantly when compared to a typical sheet-to-sheet inkjet printer [2]. Moreover, the limited number of process parameters makes print quality optimization relatively straightforward when compared to more complex systems, such as inkjet and 3D printing (let alone high-resolution electrohydrodynamic and aerosol jet printing). However, the minimum layer thickness of the screen-printed features is relatively large (i.e. order of tens of microns [61]), and in certain applications (e.g. the aforementioned ultrathin devices) this may not be acceptable. Similarly, the adaptability of this technology is not on par with,

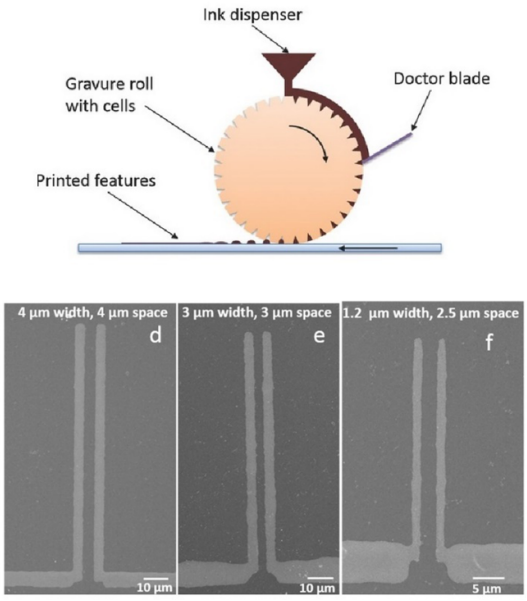

Figure 3. (A) Functioning principle of a gravure printer. [63]. John Wiley & Sons. © 2016 WILEY-VCH Verlag GmbH & Co. KGaA, Weinheim. (B) Wettability contrast gravure printing of silica nanoparticle ink lines with a minimum line width of 1.2 μm. [62] John Wiley & Sons.© 2015 WILEY-VCH Verlag GmbH & Co. KGaA, Weinheim.

for example, inkjet printing because it requires the use of a physical print mask fabricated with a multistep lithographic process, thereby preventing similar batch-to-batch customizability of the printed pattern [3]. However, this is a shortcoming mainly in rapid prototyping applications, and large-scale fabrication is not prevented by it [58, 59].

2.1.3. Gravure printing

Gravure printing is a widely used roll-to-roll printing technique for applications requiring high throughput (up to 1000 m min^{-1} [2]). A typical gravure printing setup consists of an ink bath, a gravure roll with the print pattern engraved on its surface, and an impression cylinder (see figure 3(A)). During operation, (1) the gravure roll picks up the ink from the ink bath, (2) excess ink is removed using a doctor blade, and (3) the gravure roll transfers the remaining ink onto the substrate, which is pressed against it using a soft impression cylinder. The printing method results in a relatively low line thickness (0.1–1 μm) and is therefore well suited for the fabrication of ultrathin devices. The resolution of the printing method is also highly variable: despite the typical line width of 10–50 μm [2], careful optimization of the wettability difference between the engraved cells and the lands resulted in a minimum line thickness/spacing of 1.2/1.5 μm [62] (see figure 3(B)).

2.1.4. Reverse-offset printing

Reverse-offset printing is a high-resolution roll-to-roll printing technology that finds utility especially in the fabrication of printed high-performance

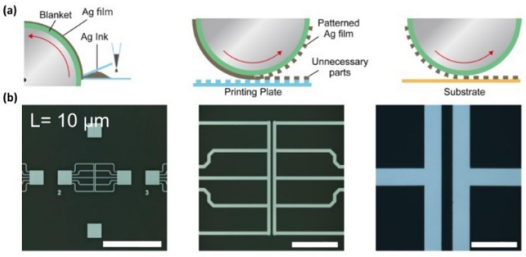

Figure 4. (A) The functioning principle of a reverse-offset printer. (B) Reverse-offset printed Ag-nanoparticle ink source/drain-electrodes with ~10 μm channel length (scale bars are 1 mm/200 μm/40 μm). Reprinted with permission from [65]. Copyright (2020) American Chemical Society.

transistors/amplifiers [64, 65]. A typical reverse-offset printer consists of a roll coated with a soft blanket made of soft polymer (e.g. polydimethylsiloxane (PDMS)) and a glass surface engraved with the print pattern [65]. During operation (see figure 4), (1) the ink is deposited uniformly on the soft blanket, (2) the blanket is pressed against the engraved glass surface, which removes the excess ink, and (3) the remaining ink (and pattern) is transferred to the substrate by pressing the blanket against it. This fabrication method enables feature sizes of 5–10 μm and line widths of a few tens of micrometers [64, 65]. Despite having a low throughput compared to other roll-to-roll printing methods, such as gravure printing (~10 mm s^{-1} [66] vs. 1000 m min^{-1} [2], respectively), it compares favorably against other high-resolution printing methods such as e-jet or aerosol jet printing (see sections 2.2.1 and 2.2.2).

2.1.5. Flexographic printing

Similar to gravure and reverse-offset printing, the flexographic printing method is based on transmission of ink onto a substrate using a printing roll with a flexible rubber relief plate. The method necessitates the use of somewhat lower viscosity inks compared to gravure and reverse-offset printing, and also results in a somewhat lower resolution and printing speed. However, the method also has certain benefits, such as a lower setup cost due to the less expensive print plates [2, 67].

2.2. Novel printing methods

Novel printing methods encompass devices developed purely for additive fabrication; that is, they do not share their origin with graphic printing tools. This includes methods developed specifically for high-resolution printing (i.e. electrohydrodynamic inkjet, aerosol jet, nanoimprint lithography), which find utility in applications where the sensor or circuit density have to be very high. In the field of on-skin biosignal monitoring, such requirements can be hypothesized to exist, for example, in the area of tactile sensors for prosthetic arms, where sensor density

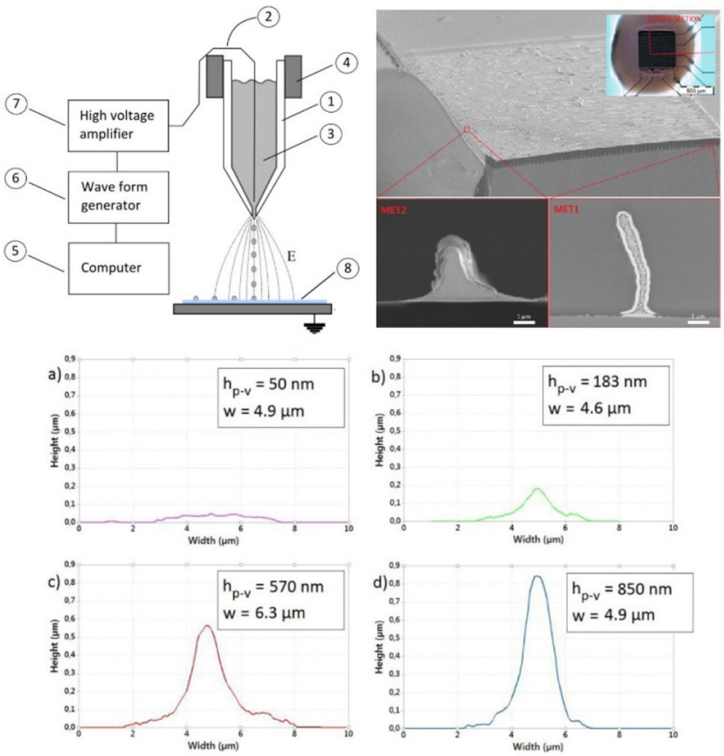

Figure 5. (A) The functioning principle of an electrohydrodynamic inkjet (e-jet) printer and an e-jet printed microelectromechanical sysstem (MEMS) package redistribution layer with 5/5 μm conductor width/spacing; scale bars are 1 μm. © 2017 IEEE. Reprinted, with permission, from [78]. (B) Multilayer e-jet printing to increase the aspect ratio of Ag-nanoparticle ink conductors: 1, 5, 10, and 15 layers. © 2015 IEEE. Reprinted, with permission, from [79].

should match the density of mechanoreceptors of human skin (i.e. 150–250 in^{-1} [68]) to accurately replicate the sense of touch; in monitoring of skin conditions for various pathologies with high spatial resolution [69]; or in heat-based blood perfusion measurements where high sensor density would be advantageous to accurately map the flow of blood [70]. Furthermore, sensor miniaturization is important in applications where it has to be placed such that it is visible to other people (e.g. electric stimulation of paralyzed facial muscles [71], pulse wave measurement from the neck artery [72], or voice recognition based on thyroid cartilage vibration [36]). Another application area is biosignal amplification, where high-resolution printing can be used to increase the performance of transistors through, for example, shorter channel lengths and source/drain–gate electrode overlaps [73].

Another technology developed purely for additive fabrication is 3D printing, which can be used, for example, to increase the complexity of printed circuits by exploiting the vertical dimension in addition to planar dimensions, and electrospinning, which can be used, for example, to fabricate porous material layers for better breathability of on-skin devices. These technologies are described in the following sections.

2.2.1. Electrohydrodynamic inkjet printing

Electrohydrodynamic inkjet (e-jet) printing is a high-resolution drop-on-demand (DoD) printing technology capable of submicrometer-scale lateral features, or an approximately 20- to 50-fold increase in resolution compared to piezoelectric inkjet printing [74]. For example, Park *et al* [75] printed ∼700 nm wide lines with polyethyleneglycol methyl ether solution using an in-house developed e-jet printing system. Interestingly, the fast evaporation of the subfemtoliter droplets can also be utilized in rapid printing of submicrometer to micrometer scale 3D features (e.g. pillars, cactus-type structures), as demonstrated by An *et al* [76]. Furthermore, e-jet printing offers more processing flexibility in terms of materials due to the higher viscosity and surface tension range of compatible inks, and in terms of print resolution, which can be controlled during the print process by varying the print parameters [74].

The functioning principle of an e-jet printer is based on an electric field-actuated droplet ejection from a narrow (∼order of μm) diameter nozzle filled with electrically functional ink (see figure 5(A)). During operation, the ink inside the nozzle is charged to a high voltage relative to the substrate surface. Initially, the electric field between the ink meniscus and the substrate causes the meniscus to take a conical

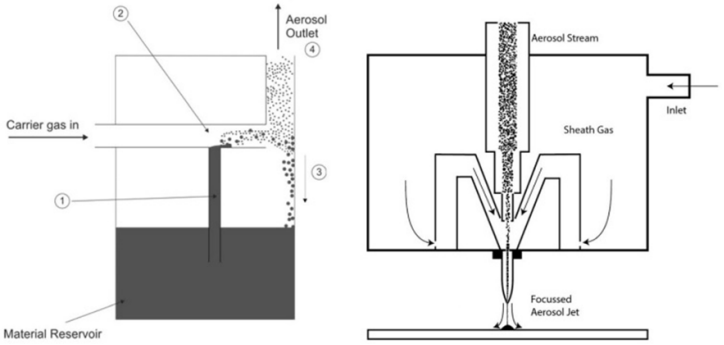

Figure 6. The functioning principle of an aerosol jet printer; atomizer (left) and printhead (right). Reproduced from [82]. CC BY 4.0.

shape (i.e. a Taylor cone). Once the strength of the electric field exceeds a threshold value, a jet of ink droplets is pulled out from the apex of the Taylor cone. Since the droplet diameter is determined by the dimensions of the Taylor cone and not the diameter of the nozzle, it may be varied to a larger extent than droplets of conventional piezoelectric inkjet printers. The droplet size variation can be achieved, for example, by varying the bias voltage, peak voltage, frequency, and waveform of the driving alternating current signal, but the interdependency of these parameters, and their effect on the resolution, is complex and must be carefully optimized depending on the substrate [74, 77].

However, the electric field-actuated droplet ejection mechanism also creates challenges, such as droplet size and print quality dependency on the electrical parameters of the dielectric substrate material (e.g. conductivity, permittivity, thickness). Similarly, charging of dielectric substrates from previously deposited layers may cause print defects during the printing of the subsequent layers [80]. Because the layer thickness scales with layer width, multilayer printing is necessary to achieve electrically functional features (e.g. conductors, pin-hole free dielectrics) [78, 79] (see figures 5(A) and (B)). A further complication is the small print height (tens to a few hundred microns), which is necessary to achieve a high-enough electric field for droplet ejection.

2.2.2. Aerosol jet printing

Aerosol jet printing is a high-resolution printing method similar to e-jet printing, but with a somewhat lower resolution of ~10 μm [81]. The functioning principle of aerosol jet printing (see figure 6) is based on the atomization of particulate ink and subsequent sheath gas-assisted collimation of the atomized ink droplets onto the substrate. This results in the most notable benefits of an aerosol jet compared to an e-jet printer: a higher print height of up to few millimeters, a higher print resolution variability of ~10 μm to a few milimeters, reduced print quality dependency on the substrate material parameters, and a larger particulate size of up to 0.5 μm. Similar to e-jet printing, the small droplet volume allows for rapid evaporation of the solvent and fast build-up of μ-3D features [82].

2.2.3. Nanoimprint lithography (NIL)

NIL is a roll-to-roll compatible high-resolution patterning method with the ability to form features at the nanoscale. The basic structure of an NIL device is very simple as it requires only two components: (1) a mold made of a high Young's modulus, abrasion resistant, and thermally stable material (e.g. silicon dioxide or -nitride, nickel); and (2) a substrate with a sufficiently low Young's modulus and viscosity. During operation, the mold is heated and pressed against the substrate, which causes the mold pattern to transfer onto the substrate. The deformation speed of the substrate material (i.e. the processing speed of NIL) increases with the substrate's decreasing Young's modulus and viscosity. Low T_g polymeric materials are especially well-suited substrate materials for NIL because their Young's modulus and viscosity drops by several orders of magnitude as they are heated above the T_g [83].

Although NIL is not a truly additive fabrication method, it can be used together with additive fabrication tools to enable high-resolution features that would otherwise be beyond their capabilities. As an example, a combination of NIL and drop-casting has been used to fabricate high-density interdigitated electrodes (IDEs) with ~10/20 μm width/spacing for a force direction sensitive P(VDF-TrFE) piezoelectric sensor [84]: NIL was used to imprint microgrooves on the P(VDF-TrFE) with a width/depth of ~10/10 μm while self-wetting of the microgrooves was exploited to fill them with a drop-casted Ag-nanoparticle ink.

2.2.4. 3D printing

Conventional printing tools are best suited for creating patterns with a relatively low aspect ratio (e.g. ~1:100 for inkjet printed one-layer Ag-nanoparticle

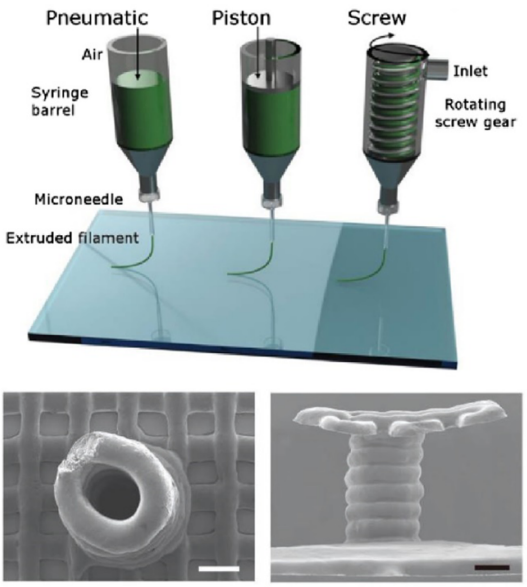

Figure 7. (A) The functioning principle of pneumatic, piston, and screw-actuated direct ink write 3D printers. [91] John Wiley & Sons. © 2019 Wiley Periodicals, Inc. (B) Three-dimensional printed sensing structures for a piezoresistive pressure sensor utilizing Ag/silicone nanocomposite ink; scale bars are 200 μm. [32] John Wiley & Sons. © 2017 WILEY-VCH Verlag GmbH & Co. KGaA, Weinheim.

conductors [55]), and the complexity of the printable systems is therefore limited by the available two dimensions. As the complexity of the electronic systems correlates with their performance (cf monolithic integration of integrated circuits (ICs) [85]), accessing the third dimension through 3D printing technology could be advantageous for achieving higher performance printed devices and to make them compatible with a wider range of applications [86–88].

Extrusion-based 3D printing (also known as direct ink writing; see figure 7(A)) is highly robust with regard to rheological parameters of the extruded liquid and allows for the use of high viscosity, high solid content functional inks, which leads to higher layer thicknesses when compared to, for example, inkjet printing technology [88]. Furthermore, the solvent evaporation time between the printing of consecutive layers can be minimized through the use of low boiling point solvents, which leads to rapid build-up of high aspect ratio structures even in an ambient environment [32] (see figure 7(B)). In its simplest form, an extrusion-based 3D printer may consist of a pressurized ink reservoir (e.g. syringe), a nozzle, and a moving substrate stage with a *xyz*-axis control [89]. The volume of extruded ink can then be controlled by varying the pressure in the ink reservoir, while the line width and thickness are controlled by the speed at which the substrate moves. In more sophisticated devices, an extruding screw is incorporated between the ink reservoir and nozzle to achieve more precise control over the volume of the extruded ink. In this case, the reservoir does not need to have separate pressure control as the extruding screw is used to pull the liquid out of the reservoir and toward the nozzle [90].

2.2.5. Electrospinning

In biosignal sensor applications, the electrospinning method is used mostly for the fabrication of layers with large coverage (i.e. substrate, capacitor dielectric, piezoelectric layers). The resulting porous nanomesh morphology can be used to engineer high air permittivity (i.e. breathability) devices, which are especially important for user comfort in the case of sensors used in long-term on-skin biosignal monitoring.

The functioning principle of electrospinning equipment is similar to e-jet printing in that the ink is loaded into a pressurized syringe/nozzle, electrically charged relative to the substrate (also called the collector plate), and ejected from the Taylor cone once a threshold electric field is exceeded (see figure 8) [92]. However, instead of an AC-, a direct current (DC) voltage is used, and this results in the ejection of a continuous stream of solution instead of separate droplets. The solvent has time to evaporate during the flight, resulting in deposition of solid fibers with a diameter of a few hundred nanometers [92]. Similar to e-jet printing, the diameter of the fiber can be controlled by controlling the driving electric field and is further affected by the rheological parameters of the solvent (e.g. surface tension, viscosity) [93].

2.3. Summary

The main process parameters and features of various printing technologies are illustrated in table 1.

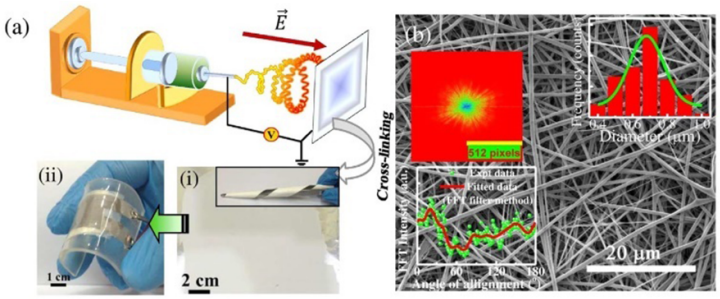

Figure 8. The functioning principle of an electrospinner (left) and an electrospun gelatin fiber nanomesh structure used as an electroactive layer in a piezoelectric pressure sensor (right). Reprinted from [19], copyright (2017), with permission from Elsevier.

Table 1. Comparison of process parameters of various printing technologies [2, 51, 81, 94].

Printing method	Ink viscosity (mN m^{-1})	Line width (μm)	Line thickness (μm)	Printing speed per layer (m min^{-1})	Print file type	Ability to print 3D structures
Piezoelectric inkjet	2–100	30–50	0.1–1	1–500	Digital	Micro-3D
Screen	500–50 000	30–50	5–100	30–150	Physical	No
Offset	100–100 000	>10	1–10	1000	Physical	No
Gravure	50–1100	10–50	0.1–1	1000	Physical	No
Flexographic	10–500	45–100	<1	500	Physical	No
Reverse offset	1–5	1–10	0.05–1	<1	Physical	No
3D direct ink writing	—	>100	—	<1	Digital	Yes
Electrohydrodynamic inkjet (e-jet)	1–10 000	>1	0.001–0.1	<1	Digital	Micro/nano-3D
Aerosol jet	1–1000	10−20	—	<1	Digital	Micro-3D
Nanoimprinting	∼0.1	>0.01	0.01	<1	Physical	Micro/nano-3D

3. Measurement principles, biosignals, and materials

Certain physiological changes in the human body result in biosignals, which can be detected noninvasively from the surface of the skin through measurement of mechanical deformation and heat transmission. Here, biosignal types are first briefly discussed on a general level and are related to specific diseases that the measurement of these biosignals may help to detect. This is followed by a section that is divided based on the physical effects (e.g. piezoelectric, capacitive) used to detect the said biosignals; this, in turn, is followed by examples of recent additively fabricated biosignal sensors utilizing the said effect.

3.1. Mechanical biosignals

Various physiological activities of the human body result in mechanical deformation, which can be measured with on-skin pressure/strain sensitive sensors [6, 8, 14–22, 26–28, 32–34, 95–98]. Biosignals that are detectable in this manner can be broadly categorized into kinematic (i.e. related to limb or muscle movement), vascular dynamic (i.e. related to the dynamics of arterial blood flow), breathing, and vocal signals [99, 100]. Kinematic biosignals measured from joints or muscles, for example, may reveal information about various movement disorders (e.g. tremors, bradykinesia, postural instability), which can be related to, for example, neurological disorders such as Parkinson's disease [101] or multiple system atrophy [102]. Other kinematic biosignals, such as foot plantar pressure distribution, can also be used for monitoring the rehabilitation progress after injury or stroke [103], diagnosis of diabetic neuropathy [104], or for monitoring the performance of an athlete [105]. In more futuristic applications, such as smart prosthetics or robotic limbs, kinematic biosignals are not only monitored but also generated and allow for, for example, replication of the human tactile sense, which may enable the fine motor control of the prosthesis/robotic limb [106].

On the other hand, biosignals related to vascular dynamics may reveal information about the health condition of the vascular system or an underlying disease, which manifests itself as an abnormality in the measured biosignal [107, 108]. For example, various parameters can be calculated from the shape of arterial pulse waves, which relate to the stiffness of the arterial system and can therefore be considered an indicator for several cardiovascular diseases (CVDs) such as coronary artery disease or cerebrovascular disease [107, 108]. Recently, it has been also proposed that pulse wave analysis (see figure 9) could help detect/prevent deadly manifestations of CVDs, such as abdominal aortic aneurysm [109]. As CVDs are

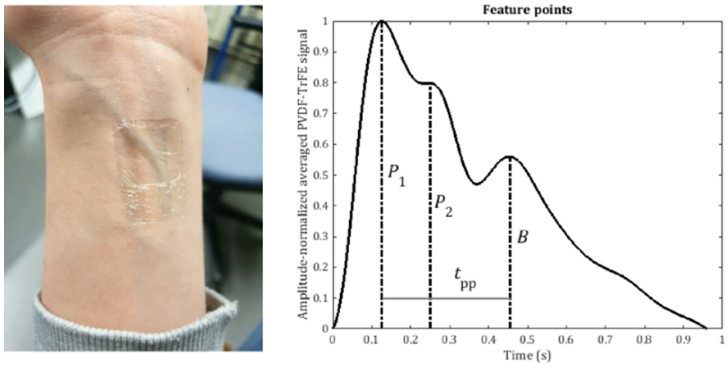

Figure 9. (A) A printed ultrathin pressure sensor attached to the wrist. © 2020 IEEE. Reprinted, with permission, from [57]. (B) Arterial pulse waves used in the evaluation of vascular health with commonly used feature points: P_1 and P_2 mark the early and late systolic wave, B is the diastolic wave, and t_{pp} is the time delay between the maximum systolic wave and B. © 2019 IEEE. Reprinted, with permission, from [17].

the most common cause of death in the world [110], their screening and prevention through cost-effective and continuous monitoring would have an enormous societal impact. As for the other mechanical biosignals, breathing-related biosignals can be used to monitor certain breathing-related disorders such as sleep apnea [111], for example, whereas detection of voice patterns (e.g. from thyroid cartilage vibration [18]) could be used for speech rehabilitation or recognition.

3.1.1. Piezoelectric effect

The piezoelectric effect is defined as a material's ability to transform mechanical energy into electrical energy (and vice versa), and materials exhibiting this effect can therefore be used in sensor applications to detect mechanical deformation. The active nature of the signal generation (i.e. direct mechanical to electrical energy conversion) makes such sensors especially interesting for applications where energy availability is limited (e.g. on-skin biosignal monitoring) [112].

In inorganic piezoelectric materials (e.g. AlN, BaTiO3, PZT), the piezoelectric effect arises from changes in the internal dipoles of the material's non-centrosymmetric crystal structure. For example, in PZT, a permanent polarization inside the unit cell is created by the shift in the location of the titanium atom relative to the center of symmetry defined by the surrounding lead and oxygen atoms. Because each crystal domain consists of repeating unit cells, there also exists a net polarization across the crystal domain. However, because the crystal domains are randomly oriented, their different polarization directions cancel each other out, thereby resulting in zero net polarization over the bulk of the material. The polarization directions of crystal domains can be aligned by applying an external electric field of sufficient strength (i.e. higher than the coercive field E_c) in a so-called poling step. When mechanical deformation is applied to the poled PZT through, for example, compressive force, the change in relative positions of the titanium atoms results in a change in the net polarization over the crystal domain and hence the bulk of the material. If the PZT is coated with a conductive material (i.e. electrode), this change will attract (or repel) free charge carriers in the electrode, which can be measured and related to the applied force. It must be noted, however, that only *changes* in force can be detected, and signal conditioning (e.g. with integrating charge or a voltage amplifier) is required to understand the quasistatic behavior of the applied force [112].

In organic piezoelectric materials (e.g. polyvinylidenefluoride (P(VDF)) and its copolymers, Poly-L-lactic acid (PLLA), gelatin, nanocellulose), the piezoelectric effect arises from the molecular dipoles in the polymer chain, which are the result of electronegativity difference between the atoms of the carbon backbone and the pendant groups. For example, in PVDF, the pendant groups consist of hydrogen and fluorine atoms and, depending on the conformation of the repeating structure (e.g. trans-trans-trans-trans, trans-gauche-trans-gauche), the unit cell of the PVDF crystalline phase may or may not exhibit permanent polarization. In PVDF, the type of chain conformation gives rise to five different crystal phases (α, β, γ, δ, ε) out of which the β-phase (with an all-trans conformation) has the highest polarization. However, organic piezoelectric materials are semicrystalline, and the crystallites are randomly oriented, resulting in zero net polarization across the bulk regardless of the crystalline phase (cf effect of crystal domains in inorganic piezoelectric materials). A poling step is therefore required to align the dipoles and to induce a net polarization across the bulk of the material. After poling, the mechanical deformation will cause a change in the net polarization over the bulk, and this can be measured using a similar approach as with inorganic piezoelectric materials [112].

Commonly used parameters to describe the performance of a piezoelectric material are: (1) the

Table 2. Solution processable and printable piezoelectric materials/nanocomposites and their performance. Piezoelectric d-coefficient $d_{33.eff}$ with units of pC/N unless otherwise indicated.

Material	E_C (V μm^{-1})	P_r ($\mu C\ mm^{-1}$)	$d_{33.eff}$ (pC N^{-1})	Processing temp. (°C)
P(VDF) [116]	50	6	−27	120
P(VDF-TrFE) [117]	50	6–7	−30	140
PLLA [95, 118]	20	9.6	$d_{14} = 18.9$	130
Gelatin (nanofibers) [19]	—	—	−20 pm V^{-1}	Room temp.
Nanocellulose [96]	—	0.15	5.7	Room temp.
Chitosan [97]	—	—	4–6	Room temp.
Diphenylalanine-derivative peptide [98]	—	—	73.1	Room temp.
β-glycine [14]	—	—	$d_{16} = 178$ pm V^{-1}	Room temp.

direct piezoelectric d_{xy}-coefficient, which relates the mechanical stress applied in the x-direction to the change in surface charge in the y-direction (unit C/N); and (2) the indirect piezoelectric d_{xy}-coefficient, which relates the applied electric field in he y-direction to the mechanical deformation in the x-direction (unit m/V). In general, inorganic piezoelectric materials have high direct piezoelectric coefficients (e.g. BaTiO3 $d_{33} = 190$ pC N^{-1}, PZT-5 H $d_{33} = 593$ pC N^{-1}, single crystal PMN-PT $d_{33} = 2000$–3000 pC N^{-1} [1, 112]), but they require very high annealing temperatures (e.g. BaTiO3 ∼600 °C [113], PZT 650 °C–750 °C [114], single crystal PMN-PT > 1000 °C [115]), which prohibits their direct fabrication onto low T_g polymeric substrates.

Recently, there have been attempts to apply these high-performance materials to on-skin biosignal sensors by employing ultrathin (and therefore highly flexible) layers through, for example, the transfer printing process. For example, transfer printing of ultrathin layers of PZT onto polyimide [69] and polyethylene terephthalate [72] substrates has been demonstrated in the fabrication of sensors for monitoring of skin pathologies and arterial pulse waves, respectively. However, transfer printing omits many benefits of truly additive fabrication technologies (e.g. throughput, customizability, selective material deposition) and cost-effective mass-scale fabrication of such devices is therefore questionable.

In contrast, organic piezoelectric materials have comparably low processing temperatures (e.g. PVDF ∼ 120 °C [116], P(VDF-TrFE) ∼140 °C [117], nanocellulose at room temperature [96]), are solution processable, and can therefore be readily fabricated on low T_g polymeric substrates using scalable additive fabrication technologies [112]. A further benefit for on-skin sensor fabrication is their biocompatibility, and, in certain cases (e.g. PLLA [118] and nanocellulose [96]), even biodegradability. However, organic piezoelectric materials suffer from low direct piezoelectric coefficients (PVDF $d_{33.eff.} = -27$ pC N^{-1} [116], P(VDF-TrFE) $d_{33.eff} = -33$ pC N^{-1} [117], nanocellulose $d_{33.eff.} = 5.7$ pC N^{-1}), which may limit the range of suitable applications [112]. Furthermore, the coercive field values for piezoelectric polymers are significantly higher compared to inorganic materials (e.g. PVDF-TrFE $E_C = 50$ V μm^{-1} [117] vs. PZT $E_C = 10$ V μm^{-1} [119]), which results in a more challenging poling process. The main performance parameters of solution processable and potentially printable piezoelectric materials are summarized in table 2.

Regarding on-skin biosignal sensors fabricated with additive fabrication technologies, Sekine *et al* proposed a simple and cost-effective screen-printing process for the fabrication of an unobtrusive radial arterial pulse wave sensor (to evaluate vascular health) with a P(VDF-TrFE) electroactive layer and PEDOT:PSS top/bottom electrodes on a 50 μm thick poly(ethylene 2,6-naphthalate) (PEN) substrate [15]. Although the measured pulse wave signal had a relatively low range (∼10 mV), the authors were able to make a distinction between early and late systolic peaks and use this information to calculate the radial augmentation index, which can be used to estimate arterial stiffness. In a follow-up study, they increased the sensitivity of the system by a factor of 10 through monolithic integration of the P(VDF-TrFE) sensor with a low-operating voltage organic pre-amplifier circuit [16] (see figure 10(A)). This system was demonstrated in the measurement of pulse wave velocity by comparing the time delay between pulses obtained from concurrent measurements at the neck and wrist arteries.

Furthermore, evaluation of fully printed P(VDF-TrFE) pulse wave sensor performance with a statistically significant number of human study subjects (22) was done by Laurila *et al* [17]. In their study (see figure 10(B)), the clinically relevant indices (radial augmentation, reflection, and stiffness index) were derived from the arterial pulse wave signals recorded with a printed device and compared to indices obtained from concurrent measurements with a reference device. The printed device was able to measure the radial augmentation index and stiffness index with good correlation to the reference sensor, thereby indicating that printed on-skin biosignal sensors have high potential for estimating the condition of the vascular system.

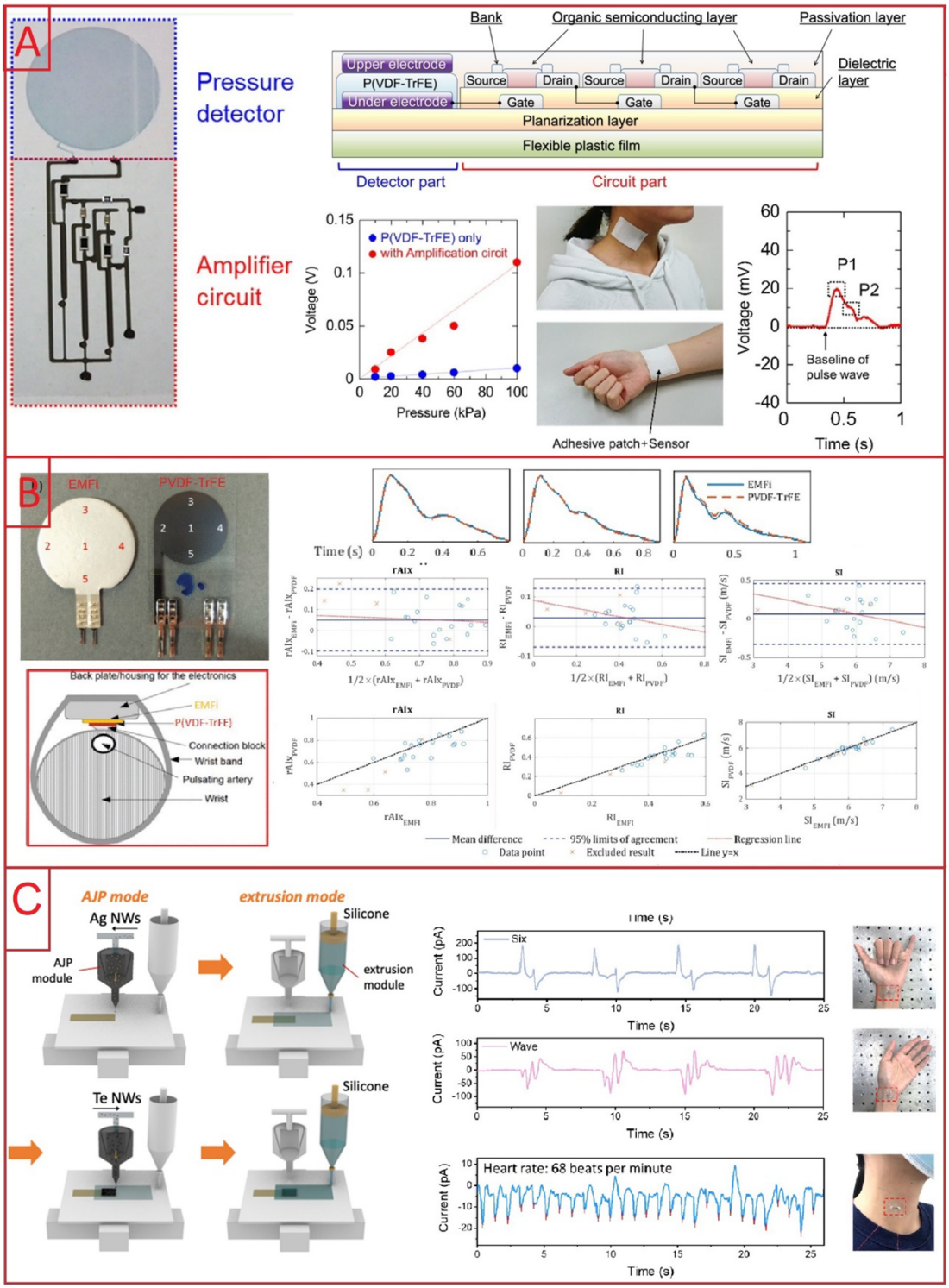

Figure 10. Recently demonstrated printed piezoelectric sensors for biosignal monitoring: (A) arterial pulse wave sensor with a screen-printed P(VDF-TrFE) electroactive layer, PEDOT:PSS electrodes, and an integrated amplifier circuit. Reprinted with permission from [16]. Copyright (2019) American Chemical Society. (B) Arterial pulse wave sensor with bar-coated P(VDF-TrFE) layer and inkjet-printed Ag- and PEDOT:PSS bottom and top electrodes. © 2019 IEEE. Reprinted, with permission, from [17]. (C) Hybrid printing of tellurium nanowire-based device with extrusion 3D printing and aerosol jet printing. Reprinted from [23], copyright (2021), with permission from Elsevier.

In contrast to devices fabricated by *in-situ* drying from solution with, for example, bar coating [17] or screen printing [16, 95]), the electrospinning process results in electroactive layers that are intrinsically stretchable. For example, biosignal sensors based on electrospun and biodegradable PLLA nanofiber meshes were fabricated by Sultana *et al* [18] and demonstrated in the measurement of arterial pulse waves, limb movement, swallowing, and voice recognition. Similarly, Ghosh *et al* [19] fabricated

sensors for arterial pulse wave and limb movement monitoring using electrospun fibers of biodegradable fish gelatin.

However, it has been noted that the electrospinning process results in random orientation of nanofibers, which may negatively affect a sensors' electromechanical performance: if the polarization direction is parallel to the lengthwise direction of the nanofiber, then randomly oriented nanofibers lead to low net polarization between charge collectors unless a separate poling step is applied [20–22]. To combat this, helix electrohydrodynamic printing (HE-printing) of P(VDF) nano/micro-fibers on pre-stretched PDMS embedded with liquid metal charge collectors was employed in the fabrication of sensors for breathing and limb movement monitoring by Huang *et al* [20]. Unlike the electrospinning process, which results in randomly oriented nanofibers, the HE-printing results in the formation of highly aligned, *in-situ* poled serpentine structures, which, coupled with out-of-plane buckling of the substrate, result in very high device stretchability of >300%. Similarly, Fuh *et al* [21] fabricated gait-sensing devices by near-field electrospinning highly aligned and *in-situ* poled P(VDF)-nanofibers on a 3D printed substrate. In contrast, Ma *et al* [22] presented a facile approach to form highly oriented electrospun P(VDF-TrFE) nanofibers for limb movement sensors by simply stretching the electrospun nanofibers after deposition. In this case, a 266% increase in the output voltage of the sensors was observed compared to sensors with randomly oriented nanofibers.

Another novel approach to increase the performance of additively fabricated piezoelectric sensors is to incorporate inorganic piezoelectric materials as nanofillers in printable piezoelectric materials. For example, Siponkoski *et al* [121] formulated a printable PZT/P(VDF-TrFE) nanocomposite ink with an indirect d_{31}-coefficient of -56 pm V^{-1}, a sevenfold increase compared to pristine P(VDF-TrFE) with d_{31} of 8 pm V^{-1}. Similarly, reduced graphene oxide [122] and nanographene oxide [123] have been used as fillers to increase the crystallinity and β-phase content of P(VDF) and P(VDF-TrFE), respectively. However, no additively fabricated on-skin biosignal sensors were realized in these studies.

In contrast, Zhou *et al* [6] demonstrated a gait-sensing device with a 3D-printed BaTiO3/P(VDF-TrFE) nanocomposite. The nanocomposite exhibited a ∼25% increase in the d_{33}-coefficient compared to pristine P(VDF-TrFE) and enabled accurate detection of foot pressure distribution, which may help with rehabilitation of leg injuries, strokes, etc. However, the performance of polymer-based piezoelectric materials can also be enhanced by changing the electrode configuration from a traditional metal–insulator–metal (MIM) to an IDE structure because the output voltage of the device is inversely dependent on the device capacitance. Yuan *et al* [24] used this approach to fabricate highly sensitive P(VDF-TrFE)-based devices with 3D printing. The authors observed that adding offset IDE structures on both sides of the piezoelectric layer increases the sensitivity 4.7-fold when compared to an MIM structure and 3.6-fold when compared to a traditional one-sided IDE structure. The device was used to detect the bending orientation of the wrist. Another interesting application of the 3D printing method was demonstrated by Du *et al* [23] (see figure 10(C)): they combined extrusion 3D printing of a stretchable silicone-based substrate with aerosol jet-printed Te-nanowire piezoelectric and Ag-nanowire electrode layers. The use of the Te-nanowires enabled a simplification of the fabrication process because this material does not need to be poled. The device was used for pulse and limb movement monitoring.

The main performance parameters of the above-mentioned devices are summarized in table 3.

3.1.2. Triboelectric effect

The triboelectric effect results from contact between two moving surfaces (of which at least one is dielectric) and concomitant charge generation onto the said surfaces. Assuming that the opposite surface of the dielectric layer is covered with a conductive material, the electrostatic screening of the generated surface charges will then cause current flow onto the dielectric–conductor interface. As the generated surface charge is proportional to the external mechanical stimuli (e.g. pressure), the measurement of the induced short circuit current reveals information about the dynamic behavior of the said mechanical stimuli. In contrast, because the dielectric surface is able to hold the generated charge for prolonged periods of time, the static (or at least quasistatic) behavior of the mechanical stimuli can be probed by measuring the open circuit voltage between the electrodes. The triboelectric effect can therefore be used in the fabrication of 'active' sensors similar to the piezoelectric effect, but with a less demanding signal conditioning system. This makes them very interesting for energy sparse applications such as on-skin biosignal measurement systems [124, 125].

There are four widely accepted triboelectric sensor architectures: the vertical contact-separation mode, the lateral sliding mode, the single electrode mode, and the freestanding triboelectric layer mode. A sensor employing the vertical contact-separation mode consists of a pair of dielectric layers with opposite triboelectric polarities stacked upon each other, while the surfaces opposite the dielectric–dielectric interface are covered with electrodes. The application of pressure perpendicular to the dielectric–dielectric interface brings the two dielectric layers into contact, thereby inducing opposite polarity charges onto their surfaces. In this case, the measurement of the open circuit voltage reveals information about the static behavior of the pressure, while the short

Table 3. Recently demonstrated printed pressure sensors utilizing the piezoelectric effect.

Biosignal	Piezoelectric layer fabrication method	Piezoelectric material	Sensitivity	Measurement range	Reference
Arterial pulse wave	Screen printing	P(VDF-TrFE)	0.6 V MPa^{-1}	0.02–1.5 MPa	[15]
Arterial pulse wave	Screen printing	P(VDF-TrFE)	1 V MPa^{-1}	10–100 kPa	[16]
Arterial pulse wave	Bar coating	P(VDF-TrFE)	0.2 V MPa^{-1}	—	[17]
Arterial pulse wave & limb movement & swallowing & voice recognition	Electrospinning	PLLA nanofibers	0 3 V MPa^{-1}	—	[18]
Arterial pulse wave & limb movement	Electrospinning	Gelatin nanofibers	0.8 V kPa^{-1}	0.3–25 kPa	[19]
Breathing & limb movement	Helix electrohydrodynamic printing	P(VDF) nanofibers	100 μA N^{-1}	0.3–13 mN	[20]
Gait sensing	Electrospinning	P(VDF) nanofibers	—	—	[21]
Limb movement	Electrospinning	P(VDF-TrFE) nanofibers	—	—	[22]
Gait sensing	3D printing	BaTiO3 + P(VDF-TrFE) nanocomposite	10 V MPa^{-1}	0.2–0.6 MPa	[6]
Arterial pulse wave	3D printing and aerosol jet	Tellurium nanowire	—	—	[23]
Limb movement	3D printing	P(VDF-TrFE)	1.47 V kPa^{-1}	4–66 kPa (pressure); 0.2–5 MPa (tensile)	[24]
Pulse wave & breathing	3D printing	P(VDF)	19 mV kPa^{-1}	up to 20 kPa	[120]

circuit current reveals information about its dynamic behavior.

A lateral sliding mode sensor closely resembles a vertical contact-separation mode sensor, except that, usually, the dielectric layers are in contact with each other. Applied shear force parallel to the dielectric–dielectric interface will then cause the two dielectric layers to slide against each other, thereby resulting in separation of the surfaces and charge generation. Micropatterned surfaces can be employed to increase the mechanical to electrical conversion efficiency by inducing multiple contact-separation cycles in a single sliding motion.

A sensor operating in a single electrode mode consists of a single electrode connected to a reference electrode or ground, and a dielectric layer. When the dielectric layer and the electrode are brought into contact with each other (through applied perpendicular or shear force), contact electrification occurs and charges move from the reference/ground electrode to the electrode to screen the induced surface charges. Due to its simple fabrication, this mode has been widely used in the fabrication of printed devices [26–28].

A sensor working in a freestanding triboelectric layer mode consists of two lateral electrodes and a freestanding triboelectric layer. During operation, the freestanding layer moves back and forth between the electrodes, thereby inducing charge on the electrodes. The main advantage of this mode is that the physical connection between the triboelectric layer and the electrodes is not necessary, resulting in reduced device wear. The triboelectric performance of different dielectric materials depends on their affinity to lose or gain electrons (i.e. triboelectric polarity) and the triboelectric pair should be made of materials of opposite triboelectric polarities to maximize device efficiency. A list of triboelectric polarities of different materials is provided by Wang in [25, 124, 125].

The use of triboelectric devices as sensors is quite a recent development, and only a few additively fabricated triboelectric biosignal sensors exist. For example, Cao *et al* [26] fabricated breathing sensors working in a single electrode mode with electrospun poly(ethylene terephthalate) (PET), polyacrylonitrile (PAN), TPU, and P(VDF) as the triboelectric layer and screen-printed Ag-nanoparticles as the electrode material. They were able to show that the device's sensitivity depends on the triboelectric polarity of the electrospun material, with P(VDF) having the highest sensitivity. They also hypothesized that electrospinning offers a natural way to form triboelectric layers with rough surfaces, which enablemultiple contact-separation cycles during single pressing of the device, and further showed that the nanomesh morphology of the triboelectric layer results in high air

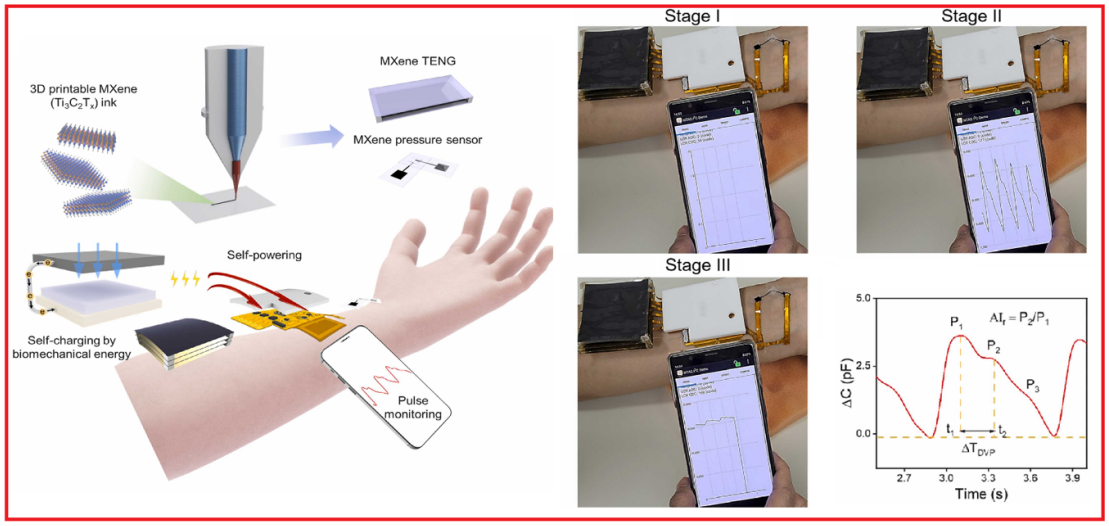

Figure 11. A recently demonstrated printed triboelectric sensor based on 3D printing of an MXene ink for a self-powered biosignal monitoring system. Reprinted with permission from [30]; copyright © 2022 Elsevier Ltd.

permeability (>6 mm s^{-1}, comparable to some fabrics), which is highly beneficial for devices meant for on-skin applications.

Similarly, Wen *et al* [27] employed screen printing to pattern graphite IDEs onto a PDMS substrate followed by drop-casting of a silk fibroin solution and used the thus fabricated multimodal sensor to monitor the breathing rate through humidity-induced permittivity change in the silk fibroin material and limb movement through the triboelectric effect between the skin and the PDMS. A triboelectric sensor based on the single electrode mode was also employed by Chen *et al* [28] for facile fabrication of a limb movement monitoring device. The fabrication process was based on a single 3D printing step of a poly(glycerol sebacate) (PGS) /carbon nanotube composite ink that formed a porous structure upon solidification and where each individual pore formed a miniature single electrode triboelectric unit. Chen *et al* hypothesized the following operation principle for their device: during deformation the exposed CNTs on the surface of the PGS pore are able to contact the PGS on the opposite side of the pore, thereby resulting in contact electrification. Because the CNTs form a conductive network through the matrix, the net effect of all the pores can be read by probing the surface of the structure. The method allowed for the fabrication of complicated 3D structures and a relatively high read-out signal of ∼4.5 V during finger movement.

Three-dimensional printing has been also employed by Zhu *et al* [29], Yi *et al* [30], Lei *et al* [31], and Yang *et al* [126] for the fabrication of triboelectric biosignal sensors. Out of these, Yi *et al*'s study (see figure 11) was especially interesting as they employed an MXene-based triboelectric device as a nanogenerator for powering all the components of the measurement biosignal measurement system, including a capacitive sensor made of the same material and an near field communication (NFC) based data transmission unit. The system exhibited a high sensitivity of 6.03 kPa^{-1} and a low detection limit of 9 Pa and thereby enabled completely self-powered and accurate arterial pulse wave monitoring.

The main performance parameters of the above-mentioned devices are summarized in table 4.

3.1.3. Piezoresistive effect

The piezoresistive effect is based on materials changing resistivity under applied stress, and can be induced by the change in the bandgap (for semiconductors such as Si or GaAs) or the change in the conduction path density (for composite materials such as PDMS/Ag-nanoparticles). As the fabrication of devices based on semiconductive piezoresistive materials requires high temperatures and micromachining techniques, this review only concentrates on the latter. Piezoresistive composite materials consist of conductive fillers embedded in a dielectric matrix, and their sensitivity to applied pressure depends on the fraction, size, shape, and material of the conductive filler together with the mechanical properties of the dielectric material (usually an elastomer). Similarly, the relationship between the applied pressure and resistivity is dependent on the size, shape, and material of the filler with high aspect ratio fillers (e.g. CNTs, nanowires) likely resulting in positive pressure coefficient piezoresistive composites (i.e. an increase in pressure results in an increase in resistance), and low aspect ratio fillers (e.g. carbon black) likely resulting in negative pressure coefficient piezoresistive (NPCP) composites (i.e. an increase in pressure results in a decrease in resistance). Considering NPCP composites, increasing pressure causes the dielectric matrix to compress, thereby increasing the probability that the conductive

Table 4. Recently demonstrated printed mechanical biosignal sensors based on the triboelectric effect.

Biosignal	Triboelectric pair fabrication method	Triboelectric pair materials	Sensitivity	Measurement range	References
Breathing	Screen printing & electrospinning	Ag-nanoparticle & P(VDF)	0.011–0.385 kPa^{-1}	2.6–400 kPa	[26]
Breathing & limb movement	Screen printing & drop-casting	Graphite & silk fibroin	—	—	[27]
Limb movement	3D printing	Carbon nanotube & Poly(glycerol sebacate)	∼0.75 V kPa^{-1}	<120 kPa	[28]
Breathing	3D printing	Resin & carbon nanotube (CNT) coated paper	—	—	[29]
Arterial pulse wave	3D printing	MXene & styrene-ethylene-butylene-styrene block copolymer(SEBS)	6.03 kPa^{-1}	9 Pa–100 kPa	[30]
Tactile	3D printing	Cu & Pectin/PDMS	3.627 kPa^{-1}	5 Pa–80 kPa	[31]
Limb movement	3D printing	Al & poly(butylene adipate terephthalate)(PBAT)	—	—	[126]

filler particles come into contact with each other. At a certain threshold compression (i.e. percolation threshold), conductive paths start to form through the composite matrix. The resistance of each parallel path is then defined by the resistance of the filler material, the constriction resistance at the interface of neighboring particles, and quantum tunneling between particles that are separated by a thin layer (<100 Å) of the dielectric material. As the compression is increased further, more and more such parallel paths are formed within the dielectric matrix and the total resistance of the material decreases according to $1/R_{tot} = \sum(1/R_1 + 1/R_2 + \ldots + 1/R_n)$, where R_n is the resistance of path n [7, 128].

Additive fabrication of piezoresistive on-skin biosignal sensors seems to be dominated by the 3D printing method. A possible explanation for this is that 3D printing is very robust with regard to rheological parameters of the ink (e.g. viscosity, surface tension), which is highly beneficial when printing elastomeric inks with a high solid content. For example, Guo *et al* [32] developed an all 3D printed, stretchable NPCP sensor to be used as a tactile or pulse rate sensor. The fabrication was based on sequential deposition of room temperature curable silicone with varying Ag-particle content. By choosing the Ag-particle content of the piezoresistive element close to the percolation threshold of 67.45 wt%, and that of the stretchable electrodes significantly higher than the percolation threshold (i.e. 75%), it was possible to minimize the resistance change of the electrodes during loading and fabricate devices with a linear pressure response from 0 to ∼125 kPa with 200-fold resistance change. The fabricated tactile sensor had a relatively high spatial resolution of ∼2 mm, which is comparable to the spatial resolution of human sense of touch at the fingertip (i.e. 0.94 mm [33]), while the pulse rate sensor was demonstrated at pulse rates of 60 and 120 beats min^{-1}. Unfortunately, the effect of stretching on the sensor's performance was not included in the study, and neither was a pulse wave analysis.

In contrast, Wang *et al* [8] minimized the effect of multidirectional forces on an all 3D printed NPCP sensor's performance by employing a porous carbon black/TPU composite to increase the sensitivity of the piezoresistive element, and designing the sensor architecture such that the stretching stress was concentrated in the IDEs and the substrate underneath the piezoresistive element. This approach resulted in only 7% resistance change upon 50% stretching, but up to 5.54 kPa^{-1} sensitivity upon compression. The hierarchical porosity of the CB/TPU composite also enabled a wide pressure range of 10 Pa to 800 kPa with different level pores responding to different pressure ranges. The device was demonstrated in measurements of radial arterial pulse waves, and clinically relevant indices (i.e. radial augmentation index, radial diastolic augmentation index) were derived from the measured pulse wave-signal and compared to reference values.

In contrast to the aforementioned devices where the materials themselves exhibit a piezoresistive effect, liquid metal Galinstan (a nonpiezoresistive material) was employed by Kim *et al* [34] for the fabrication of an NPCP-type sensor where the piezoresistive effect arises from geometrical change in the conductor dimensions (i.e. change in conductor cross-sectional area upon compression; see

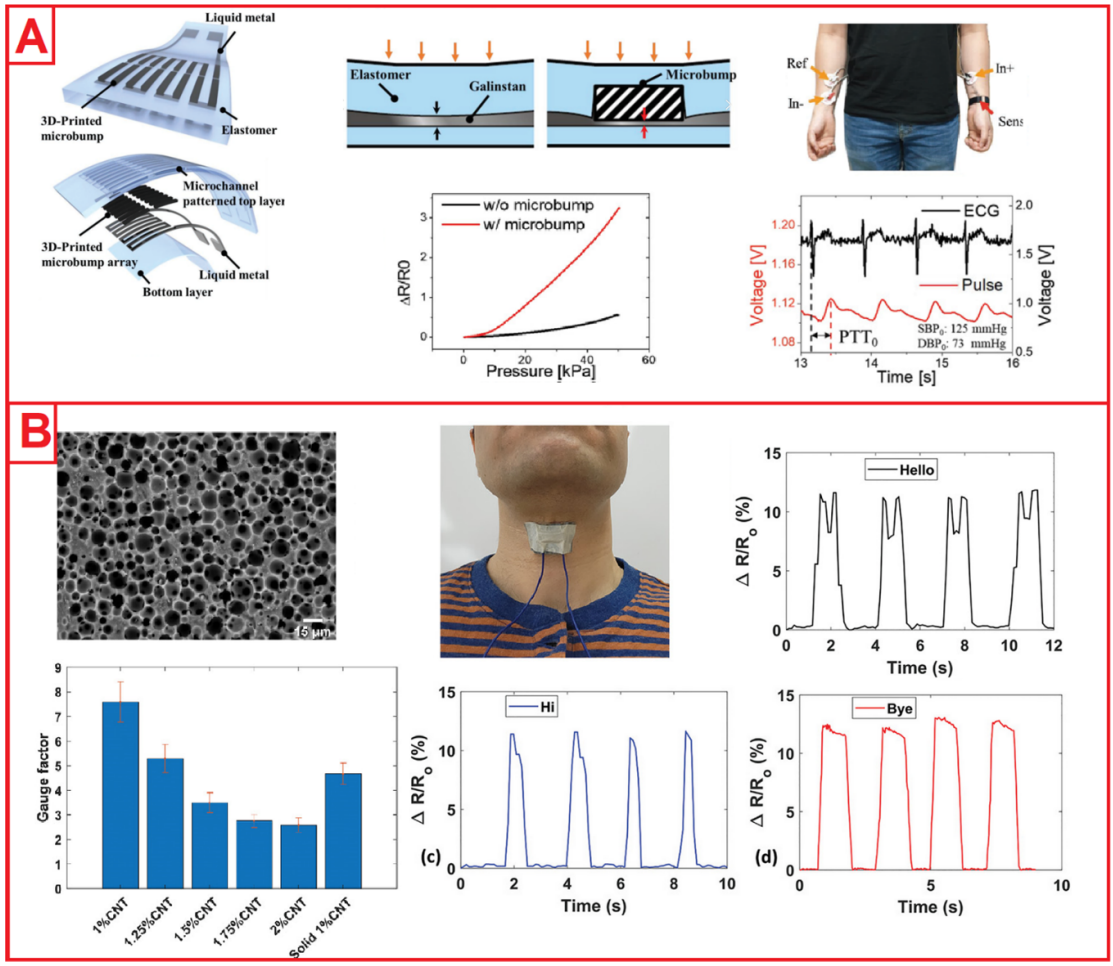

Figure 12. Recently demonstrated printed piezoresistive sensors for mechanical biosignal monitoring: (A) 3D printed liquid metal (Galinstan)-based sensor for pulse wave and blood pressure monitoring; and (B) 3D direct ink-printed CNT/PDMS-based porous conductive polymer nanocomposite (CNPC) sensor for voice recognition. (A) [34] John Wiley & Sons. © 2019 WILEY-VCH Verlag GmbH & Co. KGaA, Weinheim. (B) [35] John Wiley & Sons. © 2022 Wiley-VCH GmbH.

figure 12(A)). The device architecture consisted of a 3D printed microbump array integrated into liquid metal filled microchannels embedded in soft elastomer. By choosing the mechanical properties of the microbump and elastomer such that the former had significantly higher elastic modulus than the latter (∼3.5 GPa vs ∼175 kPa, respectively), but similar Poisson's ratios (0.35 vs. 0.499, respectively), the elastomer deformation was concentrated underneath the microbump, leading to a larger change in microchannel cross-sectional area in response to applied pressure. The device exhibited a ∼5.8-fold increase in sensitivity when compared to a device without the microbump array. The sensor's performance was further demonstrated in pulse transit time-based cuffless blood pressure measurements, where the pulse transit time was determined based on the time difference between the systolic peak of the radial arterial pulse wave obtained with the printed sensor and the corresponding R-peak obtained with a commercial electrocardiogram (ECG) measurement device.

Another approach for fabricating high sensitivity piezoresistive biosignal sensors is to use porous conductive polymer nanocomposites (CNPCs), as demonstrated by Abshirini *et al* [35] (see figure 12(B)). In their case, a 3D direct ink-writing method was employed together with evaporation-induced phase separation for the fabrication of the CNT/PDMS-based CNPC layer. The key to optimized device performance was the optimization of the pore size based on the CNT concentration, with 1 wt% CNT loading producing the highest GF of 7.6. The device was used for voice recognition.

The main performance parameters of the above-mentioned devices are summarized in table 5.

3.1.4. Capacitive effect

A simple parallel plate capacitor can act as a pressure or strain sensor if the dielectric layer is compressible enough; that is, if it has a low enough Young's modulus. For example, in pressure sensor applications, the compression of the dielectric layer will lead to a change in capacitance according to $\frac{\Delta C}{C} = \frac{2}{AE\prime}F$, where ΔC is the change in capacitance, C is the initial capacitance, A is the overlapping electrode area, $E\prime$ is the effective Young's modulus of the dielectric

Table 5. Recently demonstrated printed mechanical biosignal sensors based on the piezoresistive effect.

Biosignal	Piezoresistive layer fabrication method	Piezoresistive layer material	Sensitivity	Measurement range	Reference
Tactile & pulse rate	3D printing	Ag-particle/PDMS	$\sim 0.2\ kPa^{-1}$	100–500 kPa	[32]
Tactile & arterial pulse wave	3D printing	Carbon black/ thermoplastic polyurethane (TPU)	$5.54\ kPa^{-1}$	0.01–800 kPa	[8]
Pulse wave & blood pressure	3D printing	Galinstan	$0.158\ kPa^{-1}$	0.016–80 kPa	[34]
Voice recognition	3D printing	CNT/PDMS	7.6 (GF)	<50 kPa	[35]
Limb movement & voice recognition & pulse & breathing	3D printing	CNT/SEBS	$161.53\ kPa^{-1\prime}$; 7.24 (gauge factor, GF)	—	[127]

layer when sandwiched between rigid electrodes, and F is the applied compressive force [9]. The most common method for achieving a compliant dielectric layer is to use a low Young's modulus elastomer (e.g. PDMS [11]), but also higher Young's modulus materials can be employed if the effective Young's modulus of the layer can be tailored by, for example, increasing its porosity [12]. Moreover, using elastomer substrates and replacing rigid electrodes with stretchable conductors (e.g. Ag-nanowires [10], ionic hydrogels [36]) enables the fabrication of fully stretchable devices with skin-like mechanical properties.

An additively fabricated capacitive and stretchable biosignal sensor for tactile sensing and patellar reflex monitoring was demonstrated by Yao and Zhu [10]. The stretchable electrodes were fabricated from screen-printed Ag-nanowires, while two silicone elastomers (i.e. PDMS and Ecoflex) with high and low Young's moduli were used as the substrate and capacitor dielectric layer, respectively. The device was characterized both as a strain sensor and a pressure sensor. As a strain sensor, a gauge factor of ∼0.7 was achieved, while the linear regime extended up to 50% strain, which is higher than the maximum skin strain during normal human movement (i.e. 44.6% associated with knee joints during squatting). The strain sensor was demonstrated in the monitoring of the patellar reflex (i.e. involuntary kick motion of the leg when the patellar tendon ligament is tapped with a hammer), which can be further related to various nervous system diseases. As a pressure sensor, the device was found to have two linear measurement regimes, below 500 kPa and 500 kPa to ∼1.2 MPa, with a sensitivity of 1.62 MPa^{-1} and 0.57 MPa^{-1}, respectively.

An array of proposed pressure sensors was used to fabricate a tactile sensor, and its performance was demonstrated by detecting the location of water droplets (mass ∼ 0.06 g). An all-stretchable capacitive sensor was also demonstrated by Woo *et al* [11]. Their approach was based on microcontact printing of PDMS/CNT stretchable conductors onto a pre-patterned PDMS substrate and spin-coated Ecoflex as the dielectric layer. Interestingly, only one linear pressure regime was observed between ∼50 kPa to ∼1.2 MPa despite similar material choices to Yao *et al*'s study (i.e. PDMS substrate, Ecoflex dielectric layer). However, the strain response was observed to be similar to Yao *et al*'s study with a linear regime up to 50% strain. The device was demonstrated in the measurement of finger movement and tactile sensing with a resolution of ∼6 mm.

In contrast to the relatively high elastic modulus nanocomposite electrodes employed in the aforementioned publications, ionic hydrogels can be used to achieve an exact match between the elastic moduli of the electrodes and the skin. Yin *et al* [36] proposed a photopolymerization-based 3D printing process for polyacrylamide - poly(ethylene glycol) (PAAm-PEGDA) hydrogel electrodes and used these to fabricate capacitive pressure sensors for voice recognition and monitoring of limb movement and pulse rate (see figure 13(A)). The co-crosslinking of two hydrogels with different mechanical properties allowed the tuning of the hydrogel electrode elastic modulus with a 280:1 AAm/PEGDA molar ratio ($E = 156.7 \pm 7.8$ kPA) resulting in a very close match to the elastic modulus of the skin ($E =$ 150–250 kPA [130, 131]), low resistance change of <8% upon uniaxial stretching of >50%, and more-than-sufficient maximum stretchability of ∼600%. Three sensors with varying hydrogel electrode topography (i.e. planar, 200 μm wide grooves, 400 μm grooves) were fabricated, and it was found that increased groove width increases the sensitivity, with 400 μm grooves resulting in a maximum pressure sensitivity of 0.84 kPa^{-1} and a strain gauge factor of 0.92. Interestingly, the transparent device was able to detect the words 'Hi' and 'Sensor' when attached to the thyroid cartilage of the test subject, thereby showing promise as an unobtrusive tool for phonation rehabilitation.

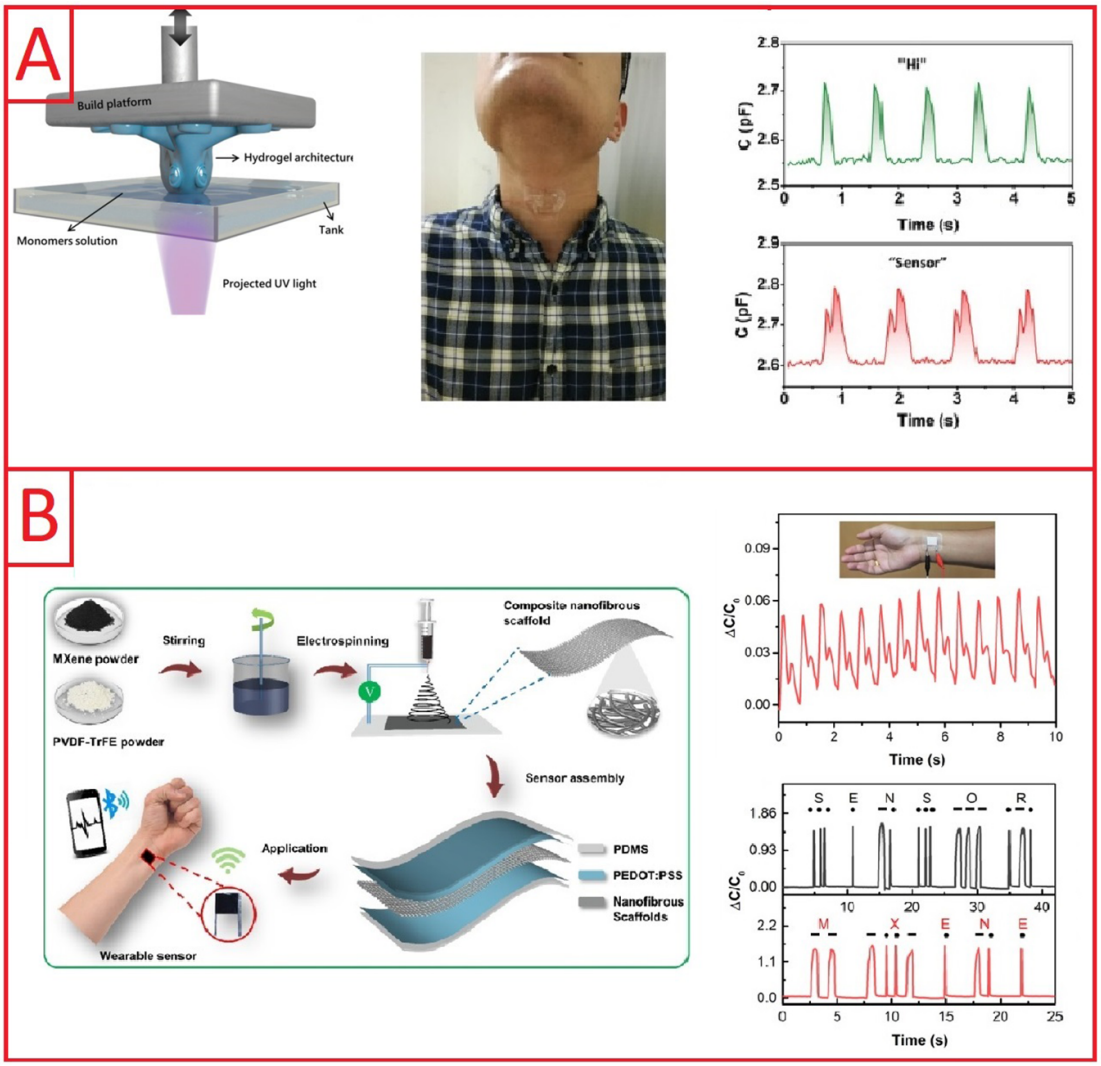

Figure 13. Recently demonstrated printed capacitive sensors for mechanical biosignal monitoring: (A) 3D printed PAAm/PEGDA hydrogel sensor for voice recognition and pulse rate monitoring; and (B) an electrospun P(VDF-TrFE)/MXene nanocomposite-based sensor for pulse wave monitoring and voice recognition. (A) Reproduced from [36] with permission from the Royal Society of Chemistry. (B) Reprinted with permission from [129]. Copyright (2020) American Chemical Society.

In addition to matching mechanical properties, optimal on-skin sensors need to be sufficiently breathable if they are to be worn continuously. Regarding this, Yang *et al* [12] developed a highly porous nanofiber mesh-based capacitive sensor by utilizing electrospun PVDF and TPU for the substrate and capacitor dielectric layers, respectively, and screen-printed Ag-nanowires for the electrodes. The sensor with the highest TPU porosity (i.e. least dense nanofiber network) exhibited the highest pressure sensitivity of 4.2 kPa^{-1} at a low pressure range (0–4 kPa), and 0.071 kPa^{-1} at a high pressure range (4–30 kPa) with a low response time of 26 ms. The high porosity of the electrospun layers resulted in a relatively high Gurley value (i.e. air permeability) of 17.3 s/100 ml. The sensor was demonstrated in the measurement of heart rate before and after exercise, and as a tactile sensor with a resolution of ∼4 mm. Similarly, Sharma *et al* [129] fabricated capacitive pressure sensors from an electrospun P(VDF-TrFE)/MXene nanocomposite (capacitor dielectric layer), spin-coated PEDOT:PSS (stretchable electrodes), and PDMS (stretchable substrate; see figure 13(B)). The introduction of 5 wt% MXene into the electrospun P(VDF-TrFE) nanofibers reduced the elastic modulus of the capacitor dielectric layer by 58% and increased its dielectric constant by a factor of 40 when compared to pristine P(VDF-TrFE) nanofiber mesh. This resulted in a 0.51 kPa^{-1} sensitivity in the low pressure regime (0–1 kPa); that is, a 4.25-fold increase when compared to pristine P(VDF-TrFE). The sensor was demonstrated in the measurement of radial arterial pulse waves and the three characteristic peaks (i.e. D-wave, T-wave, and P-wave) required for the calculation of clinically relevant indices were clearly visible in the obtained pulse wave-signal. The sensor's performance was further demonstrated in voice recognition and monitoring of involuntary eye twitching.

The main performance parameters of the above-mentioned devices are summarized in table 6.

Table 6. Recently demonstrated printed mechanical biosignal sensors based on the capacitive effect.

Biosignal	Additive fabrication method	Additively fabricated layer/material	Sensitivity	Measurement range	Reference
Tactile & patellar reflex	Screen printing	Electrodes: Ag-nanowire	1.62 MPa^{-1}	<0.1–1.4 MPa	[10]
Tactile & limb movement	μ-contact printing	Electrodes: CNT/PDMS nanocomposite	—	<0.1–1.2 MPa	[11]
Voice recognition & pulse rate	3D printing	Electrodes: PAAm/PEGDA ionic hydrogel	0.91 kPa^{-1}	0.012–2 kPa	[36]
Tactile & pulse rate	Electrospinning (substrate and dielectric) + screen printing (electrodes)	Substrate: PVDF; electrodes: Ag-nanowire; dielectric: TPU	4.2 kPa^{-1}	0.0016–32 kPa	[12]
Arterial pulse wave & voice recognition & eye twitching	Electrospinning	Dielectric: P(VDF-TrFE)/MXene nanocomposite	0.51 kPa^{-1}	0.0015–300 kPa	[129]

3.2. Thermal biosignals

The function of the body's thermoregulation system is to contribute to the maintenance of homeostasis (i.e. optimal working conditions of the organs) by controlling the body's core temperature with an accuracy of a few tenths of a degree [132]. Slight deviations from the expected body core temperature reveal changes in the homeostasis as a response to, for example, viral/bacterial infections or other diseases, and its accurate measurement therefore provides a window to observe the health status of an individual. Furthermore, body core temperature changes can be related to changes in the cognitive status of the individual, for example, being awake vs. asleep [133] and detecting different phases of sleep [134]. Since the thermal mass of the body is large, these changes occur slowly, and the time response of the measurement device may also be slow. However, further information about health status may be obtained through monitoring of transient thermoregulation mechanisms such as vasoconstriction and -dilation, which create spatiotemporal temperature changes on the surface of the skin and reveal information about the condition of the vascular system [132, 135]. Similarly, spatiotemporal temperature changes may be caused by various diseases/conditions, for example breast cancer [136], diabetes [137], bowel ischemia, liver disease, and dermatologic conditions (e.g. wound healing) [135]. As these changes require both spatial and temporal temperature mapping (see figure 14), the measurement device needs to have low thermal mass to enable a relatively fast time response and a high sensor density to enable high spatial accuracy. The low thermal mass is also important so that the sensor does not affect the measured signal by enhancing or suppressing natural cooling of the skin.

The thermal accuracy of current medical thermometers is very high (order of a few tenths of a degree), but they are limited in their time response due to their bulky size and resulting large thermal mass [37]. Such devices are well suited for single time measurement of body core temperature, but are not convenient for long-term monitoring. Similarly, infrared thermography, the golden standard for spatiotemporal temperature mapping, is bulky, expensive, and not suitable for long-term monitoring. Recently, skin-conformable and low thermal mass on-skin temperature sensors fabricated with cost-effective additive fabrication technologies have been proposed to solve these issues and to enable long-term monitoring of the aforementioned physiological signals.

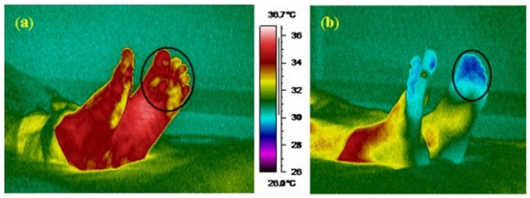

Figure 14. Examples of typical thermographic images of plantar region of two diabetic subjects with (a) and without (b) plantar neuropathy. Reprinted from [135], copyright (2012), with permission from Elsevier.

3.2.1. Thermoresistive effect

The structural simplicity of thermoresistive temperature sensors has made them especially appealing for additive fabrication. The thermoresistive effect results from the temperature-dependent variation of resistance according to $\frac{\Delta R}{R} = \frac{\Delta \rho}{\rho} - \alpha \Delta T$, where R is the resistance, ρ is the resistivity, α is the thermal expansion coefficient, and T is the temperature. In conventional thermoresistive materials (e.g. pure metals, inorganic semiconductors), the geometric effect ($\alpha \Delta T$) is very small compared to the change in resistivity ($\Delta \rho / \rho$) and can therefore be neglected. In this case, the thermal coefficient of resistance (TCR) is simply $TCR = \frac{\Delta R}{R}\frac{1}{\Delta T} = \frac{\Delta \rho}{\rho}\frac{1}{\Delta T}$ (units ppm K^{-1}). The mechanism behind the resistivity change differs

depending on the material and may cause either an increase in resistance with increasing temperature (i.e. positive TCR or PTCR) or a decrease in resistance with increasing temperature (i.e. negative TCR or NTCR). Metals generally exhibit linear PTCR behavior due to increased electron scattering at elevated temperatures, whereas semiconductors generally exhibit more complex behavior with alternating NTCR and PTCR regions due to the nonlinear relationship between the temperature and carrier concentration/mobility.

Recently, the use of carbon-based materials (e.g. graphite, graphene, CNT), conducting polymers (e.g. PEDOT:PSS), and their nanocomposites have been proposed to increase the biocompatibility of thermoresistive sensors and to enable a better match between the mechanical properties of the sensor and the skin. Various theories have been proposed to explain the origin of the thermoresistive effect in these novel materials (e.g. percolation, conduction pathway, hopping transport, tunnel effect, and electric field emission) but no clear consensus has yet been reached as to which are the dominant mechanisms. Furthermore, polymers in general have a relatively high thermal expansion coefficient, and the geometric effect on the TCR cannot be fully neglected, similar to pure metals or semiconductors. The application of these novel materials in on-skin biosignal monitoring systems also creates certain engineering challenges such as the sensitivity of conducting polymers (especially PEDOT:PSS) to changes in environmental factors (e.g. humidity) or the sensitivity to deformations transferred from the skin to the sensing element by skin-conformable substrates. Nevertheless, skin-like mechanical properties, increased biocompatibility, eco-friendliness, and compatibility with facile additive fabrication technologies have made them interesting alternatives for on-skin biosignal sensors [37, 139].

Honda *et al* [38] employed a nanocomposite ink of PEDOT:PSS and CNTs to fabricate a fully printed temperature sensor for multifunctional smart bandages (other components included a printed capacitive touch sensor, a PDMS micropump for drug delivery, and a printed antenna). The temperature sensor exhibited NTCR-type behavior between 22 and 50 °C with a TCR of −6600 ppm K^{-1}. Interestingly, the obtained TCR value was significantly higher than the TCRs of the ink components: for pure PEDOT:PSS and CNT the TCRs were −4000 ppm K^{-1} and −1800 ppm K^{-1}, respectively. The physical mechanism behind the synergistic effect was related to electron hopping between CNT particles in the PEDOT:PSS matrix. Similarly, Yamamoto *et al* [39] fabricated a multifunctional smart bandage with a printed PEDOT:PSS/CNT nanocomposite temperature sensor integrated with CNT-based thin film transistor (TFT). The sensitivity of the integrated TFT/temperature sensors was evaluated to be −8900 ppm K^{-1} between 27 and 45 °C. Nakata *et al* [40] achieved similar performance using a PEDOT:PSS/CNT nanocomposite temperature sensor integrated with ion-sensitive field effect transistor (FET) (TCR of −8500 ppm K^{-1}).

Despite the proposed use in on-skin biosignal measurement applications, where environmental factors may change drastically during use, none of the said studies evaluated the humidity stability of the device. Regarding this, Vuorinen *et al* [41] fabricated an all-printed PEDOT:PSS/graphene nanocomposite temperature sensor on a skin-conformable substrate (see figure 15(A)). The device consisted of an inkjet-printed thermoresistive component, screen-printed silver electrodes, and a stretchable polyurethane substrate. When characterized in an inert argon atmosphere, the sensor had a temperature regime of 34 °C–44 °C with a TCR of −6000 ppm K^{-1}. However, when moved to an ambient atmosphere, the same sensor exhibited PTCR behavior with high levels of drift and exhibited highly linear NTCR behavior with negligible hysteresis. The change in sensor behavior was associated with the effect of humidity on the charge transport properties of the PEDOT:PSS polymer matrix; humidity-induced change from electronic to ionic charge transport was identified as a possible underlying mechanism. An encapsulating humidity barrier material was dispensed onto the thermoresistive component resulting in NTCR behavior and reduced hysteresis in an ambient environment, thereby highlighting the importance of encapsulation to ensure proper function of PEDOT:PSS-based temperature sensors.

In a more recent contribution, Wang *et al* [42] proposed a fully printed PEDOT:PSS-based temperature sensor with high humidity stability by adding a cross-linker (GOPS) and surfactant to the PEDOT:PSS and encapsulating the device with a fluorinated polymer passivation layer (poly[perfluoro(4-vinyloxy-1-butene)] (CYTOP); see figure 15(B)). The addition of GOPS to the PEDOT:PSS at a weight ratio of over 5:1 was observed to reduce the resistance change from between 30% RH and 80% RH to ∼5%, while further addition of CYTOP encapsulation reduced it to a negligible value. The sensor with optimum GOPS to PEDOT:PSS concentration (9:1) was characterized in an ambient environment between 30 and 45 °C and exhibited a TCR of −7700 ppm K^{-1} with a high degree of linearity and negligible hysteresis up to 10 000 cycles.

As a more robust material against changing environmental factors, Ag-nanoparticle ink-based temperature sensors were proposed by Vuorinen *et al* [13]. The thermoresistive component was highly miniaturized (area <1 mm^2) by using an e-jet printing method to ensure unobtrusiveness of the device and increased user-comfort in long-term on-skin measurements. Furthermore, the patient safety and eco-friendliness

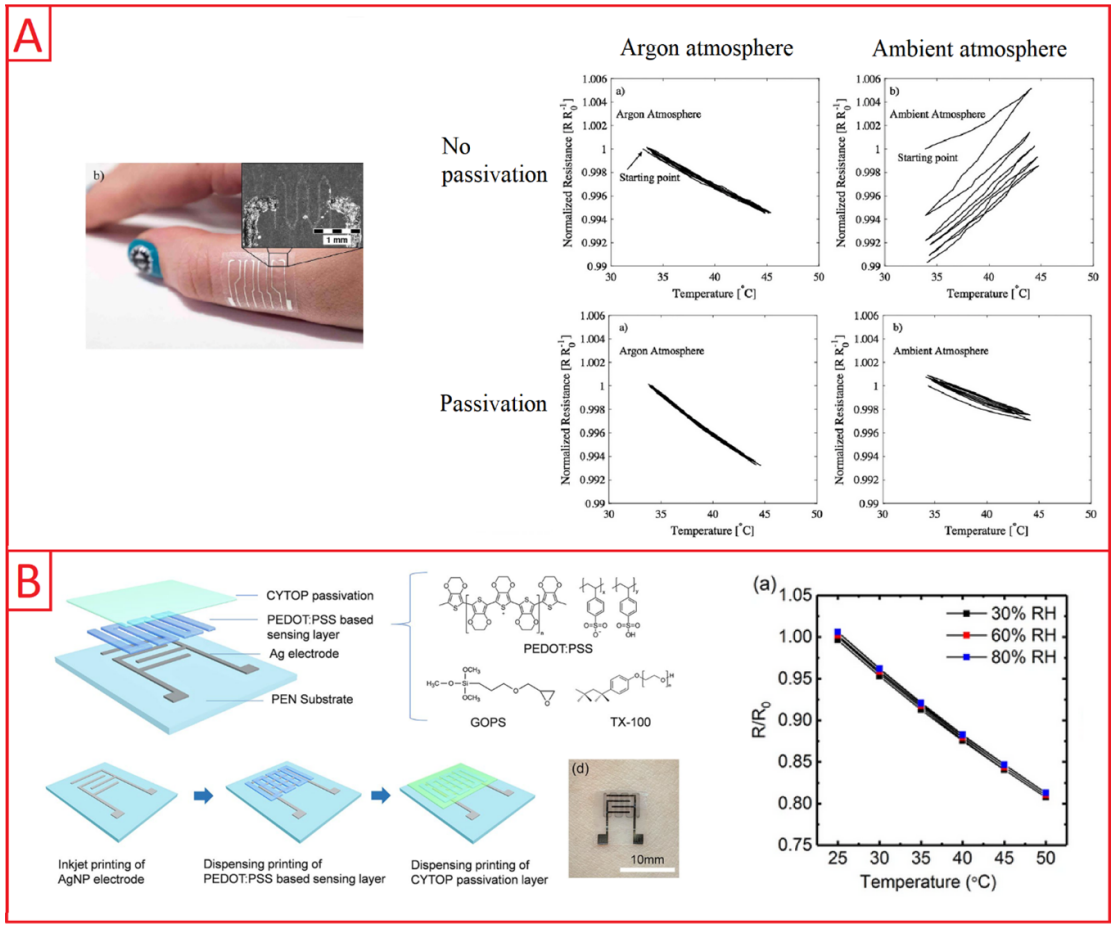

Figure 15. Recently demonstrated printed thermoresistive sensors for thermal biosignal monitoring: (A) inkjet- and screen-printed PEDOT:PSS/CNT nanocomposite thermal sensor w/wo passivation; and (B) inkjet-printed and dispensed high humidity stability sensor based on a cross-linked PEDOT:PSS sensing layer and Ag-nanoparticle electrode material. (A) Reproduced from [41]. CC BY 4.0. (B) Reproduced from [42]. CC BY 4.0.

of the device was enhanced by using a biodegradable bacterial nanocellulose substrate instead of commonly used synthetic polymer substrates. The sensor was characterized between 24 and 41 °C and resulted in a TCR of 602 ppm K^{-1}. Compared to PEDOT:PSS nanocomposite sensors, the obtained TCR was an order of magnitude lower, which partly explains the high interest in the development of printed polymer nanocomposite-based temperature sensors.

Unlike the previously mentioned studies, Wang *et al* [43] also considered the mechanical stability of the sensor's performance when designing their 3D-printed stretchable temperature sensor. The strain stability of the PDMS/graphene nanocomposite-based sensor was improved by using a millimeter scale cellular structure achieved with a direct 3D ink-writing technique. It was possible to increase the strain stability by varying the geometry of the cells from solid to hexagonal to triangular to grid structure; at 20% strain, 15% and 90% change in sensitivity were observed for the most stable (grid) and least stable (solid) structures, respectively. The TCR value of the cellular sensors measured between 25 and 75 °C was 8000 ppm K^{-1}.

The abovementioned devices can detect local changes in temperature, but the spatial temperature mapping required—for example, in blood perfusion measurements—is not possible. Regarding this, Katerinopoulou *et al* [138] demonstrated a fully printed temperature-sensing array based on a nanocomposite ink consisting of thermoresistive ceramic manganese spinel oxide particles in a benzocyclobutene polymer matrix. The high TCR of the ceramic particles resulted in a nanocomposite thermal constant of 3500 K at −93 to +67 °C, which is on par with the thermal constant of bulk ceramics. To compare with the other printed devices of this review, a TCR of −9170 ppm K (in a temperature range of 40 °C–140 °C) was calculated from the data provided in the article.

The main performance parameters of the abovementioned devices are summarized in table 7.

3.2.2. Other

In addition to the thermoresistive effect, thermoelectric and capacitive effects have been employed in the fabrication of printed temperature sensors. The thermoelectric effect is based on a temperature

Table 7. Recently demonstrated printed thermal biosignal sensors for body temperature monitoring based on the thermoresistive effect.

Additive fabrication method	Thermoresistive layer	Thermal coefficient of resistance	Temperature range	Reference
Stencil printing	poly (3,4-ethylenedioxythiophene)-poly (styrenesulfonate) (PEDOT:PSS)/CNT nanocomposite	−6600 ppm K^{-1}	22–50 °C	[38]
Screen printing	PEDOT:PSS/CNT nanocomposite	−8900 ppm K^{-1}	27–45 °C	[39]
—	PEDOT:PSS/CNT nanocomposite	−8500 ppm K^{-1}	29–44 °C	[40]
Inkjet printing/screen printing	PEDOT:PSS/graphene nanocomposite	−6000 ppm K^{-1}	34–44 °C	[41]
Inkjet printing/ dispensing	PEDOT:PSS (3-glycidyloxypropyl)trimethoxysilane (GOPS) mixture	−7700 ppm K^{-1}	30–45 °C	[42]
E-jet printing/screen printing	Ag-nanoparticle ink	602 ppm K^{-1}	24–41 °C	[13]
3D printing	PDMS/graphene nanocomposite	8000 ppm K^{-1}	25–75 °C	[43]
Inkjet printing/stencil printing	Carbon black	375 ppm K^{-1}	28–50 °C	[44]
Screen printing	Benzocyclobutene/ manganese spinel oxide nanocomposite	−9170 ppm K^{-1}	−93–67 °C	[138]

gradient-generated electric potential difference between two conductors with different Seebeck coefficients, whereas the capacitive effect results from the thermal expansion of the dielectric layer in parallel plate capacitor-type sensor structures. Regarding the former, Zhu *et al* [141] employed polyaniline nanocomposites (42.6 μV K^{-1}) and a silver paste (0 μV K^{-1}) to fabricate a temperature-sensing array for on-skin temperature mapping. The measured thermoelectric sensitivity of the sensor element was 109.4 μV K^{-1}, but the temperature range was not disclosed. Regarding the latter, the high thermal expansion of hydrogels was used by Lei *et al* [45] to fabricate 3D-printed capacitive temperature sensors. However, the capacitive sensors had a narrow linear regime from 28 to 36 °C, and the temperature sensitivity was not disclosed, so it remains unclear if the capacitive-type devices have the potential for body temperature measurements.

4. Emerging field of additively fabricated electronic tattoo-type mechanical and thermal biosignal sensors

Electronic tattoo (e-tattoo)-type devices are extremely thin (t <10 μm) electronic devices that have recently been proposed to realize highly skin-conformable and imperceptible biosignal sensors [46–48]. In addition to enhanced user comfort, these devices promise to introduce new measurement functionalities (e.g. cuffless arterial pulse wave measurements, more accurate tracking of the skin temperature), which are not attainable with traditional 'thick' on-skin sensors. However, as e-tattoo type devices are going to be disposable due to their fragility (arising from their minimal thickness), the development of cost-effective and scalable fabrication methods is needed to enable their large-scale deployment. Despite this strong motivation for utilization of printing methods in e-tattoo fabrication, only a few fully printed mechanical and thermal sensors have been demonstrated (see table 8).

Regarding mechanical e-tattoo sensors, Wang *et al* [46] demonstrated the cuffless measurement of arterial pulse waves from the wrist artery using a fully printed P(VDF-TrFE)-based piezoelectric pulse wave sensor (see figure 16). The device was fabricated on a thin parylene-C substrate using inkjet printing and bar coating and transferred to the skin using temporary tattoo paper. The proposed cuffless measurement mode was enabled by the ultrathin form factor of the device (t = 4–5 μm), which allows the device to bend together with the skin during arterial pulsation. This, in turn, enabled access to the high bending mode sensitivity of the P(VDF-TrFE) piezoelectric layer, thereby increasing the signal-to-noise ratio approximately 50-fold when compared to traditional arterial tonometry where only normal

Table 8. Recently demonstrated printed electronic tattoo-type mechanical and thermal biosignal sensors based on the thermoresistive effect.

Biosignal	Additive fabrication method	Additively fabricated layer/material	Sensitivity	Measurement range	Reference
Arterial pulse wave	Inkjet printing & bar coating	Electrodes: PEDOT:PSS Piezoelectric layer: P(VDF-TrFE)	1703 pC N^{-1}	3.2 kPa–6.4 kPa; 0.04–0.08 N	[46]
Arterial pulse wave & limb movement	Inkjet printing & bar coating	Electrodes: PEDOT:PSS Piezoelectric layer: P(VDF-TrFE)	38 pC N^{-1}; 7491 mV N^{-1}	0.1–0.5 N	[50]
Limb movement & skin temperature	Electrospinning	Piezo/-thermoresistive layer: polyvinylalcohol (PVA)/gold nanomesh	—	1–9 Pa	[140]

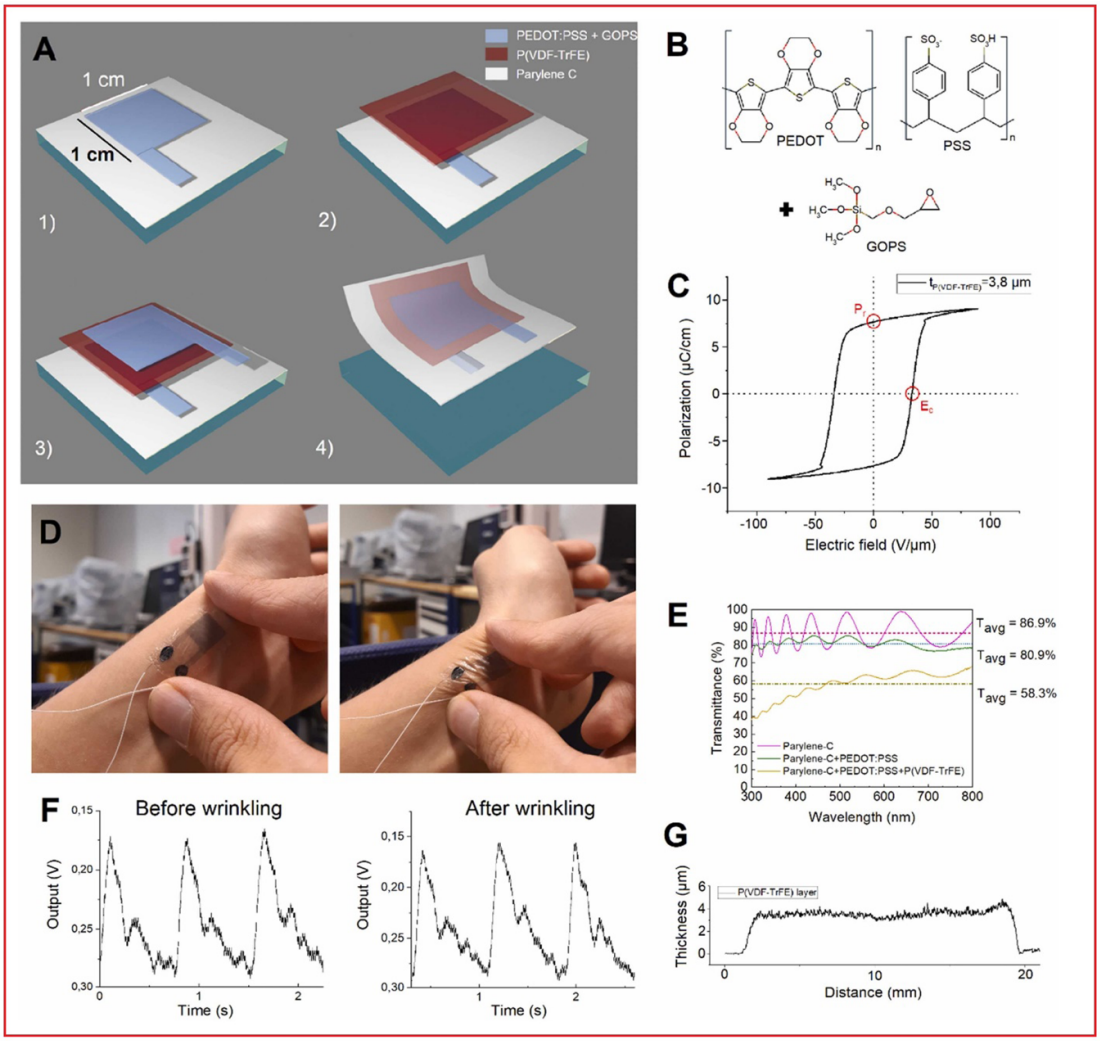

Figure 16. Recently demonstrated fully printed (inkjet printing and bar coating) electronic tattoo sensor for arterial pulse wave monitoring. Reproduced from [49]. CC BY 4.0.

forces are present. The sensor's pulse wave measurement performance was validated by comparing the signal to that obtained with a finger cuff-based reference measurement. Interestingly, it was observed that the success of the cuffless measurement varies significantly depending on the study subject, with the variation in the wrist anatomy specified as the likely cause. Similarly, Lozano Montero *et al* [50] demonstrated successful cuffless arterial pulse wave measurement using a P(VDF-TrFE)-based ultrathin (t ∼5 μm) sensor. In this case, the device utilized inkjet-printed IDEs instead of the traditional MIM structure. The study showed that the use of an IDE structure results in increased thickness, normalized voltage sensitivity, and the ability to detect bending orientation. In addition to pulse wave measurements,

the device was also used to detect limb movement. It is possible to combine mechanical and thermal measurements in a single e-tattoo device, as demonstrated by Miyamoto *et al* [140]. The active layer of their device consisted of an electrospun PVA nanomesh coated with a gold conducting layer, which acted both as a piezoresistive layer for measuring strain/-pressure and as a thermoresistive layer for measuring heat.

5. Conclusions and outlook

This review paper has discussed the recent advances in additively fabricated mechanical and thermal on-skin biosignal sensors. Based on this, we may draw certain conclusions about the current status of the field, and make proposals for its future development.

1) Sheet-to-sheet vs. roll-to-roll: the printing technologies employed so far are heavily focused on sheet-to-sheet methods (e.g. screen, 3D printing, inkjet printing), while roll-to-roll methods (e.g. gravure, flexographic) are nonexistent in this field. To fully leverage the additive fabrication methods' scalability, the use of the latter should also be explored.
2) System integration: in most cases, the presented studies propose a fabrication method for a *sensor element.* However, a fully functional biosignal sensing system also requires many other components to work independently (e.g. pre-amplifiers (see also the point below), energy harvesting/storage units, data transmission units). It is therefore important to explore the integration of these components (printed if possible) with printed sensor elements.
3) Integrated signal processing circuits: similar to the above point, sensor elements also require signal conditioning to process the biosignals properly. Pre-amplifiers with printed transistors should have more than sufficient performance in this domain because the measured biosignals contain the relevant information at relatively low frequencies (e.g. arterial pulse waves contain clinically relevant information in a narrow bandwidth of only ∼50 mHz to 50 Hz).
4) Power consumption: resistive and capacitive sensors offer good performance, but their main shortcoming is rarely discussed; that is, they are relatively power hungry. This is problematic, because the long-term goal of the field is to develop solutions for continuous vital-sign monitoring, which necessitates wireless and battery-free operation of the system and, at the same time, the available energy for mechanical energy harvesting from the human body is very limited. Self-powered devices (e.g. triboelectric or piezoelectric) offer a more straightforward path to the ultimate goal because they can be used both for harvesting mechanical energy and as low-power sensors for biosignal measurement. For fair comparison, it would be good to also state the energy consumption of nonself-powered (e.g. capacitive, piezoresistive) devices.
5) Skin-conformability: as mentioned in the introduction, one of the major motivations in developing additive fabrication processes for on-skin biosignal sensors is their ability to utilize skin-conformable materials. However, very few studies in fact measure skin-conformability despite citing it as one of the main 'selling points' of the study. One potential reason for this is the lack of any standardized test method to quantify skin conformability, and it would therefore be highly beneficial to develop/agree upon such a method.
6) Biosignal validation: although the situation seems to be improving quickly, the validation of the obtained biosignal with proper methods is still a clear shortcoming in this field. At the very least, proper validation necessitates (a) a significant number of study subjects and (b) a concurrent reference measurement with a golden standard method.

Data availability statement

The data cannot be made publicly available upon publication because they are owned by a third party and the terms of use prevent public distribution. The data that support the findings of this study are available upon reasonable request from the authors.

Acknowledgments

The author would like to thank Professor Matti Mäntysalo for helpful discussions regarding the manuscript and acknowledge the financial support by H2020 Marie Skłodowska-Curie Actions (MSCA) Individual Fellowship (IF) Grant UNOPIEZO (Grant No. 10102243).

ORCID iD

Mika-Matti Laurila https://orcid.org/0000-0002-8073-1895

References

[1] Cui Z 2016 *Printed Electronics: Materials, Technologies and Application* (New York: Wiley)
[2] Fukuda K and Someya T 2017 *Adv. Mater.* **25** 1602736
[3] Hutchings I M and Martin G D 2013 *Inkjet Technology for Digital Fabrication* (New York: Wiley)
[4] Suikkola J, Björninen T, Mosallaei M, Kankkunen T, Iso-Ketola P, Ukkonen L, Vanhala J and Mäntysalo M 2016 *Sci. Rep.* **6** 25784
[5] Liang J, Tong K and Pei Q 2016 *Adv. Mater.* **28** 5986–96

[6] Zhou X, Parida K, Halevi O, Liu Y, Xiong J, Magdassi S and Lee P S 2020 *Nano Energy* **72** 104676
[7] Ruschau G R, Yoshikawa S and Newnhamn R E 1992 *J. Appl. Phys.* **72** 953
[8] Wang Z, Guan X, Huang H, Wang H, Lin W and Peng Z 2019 *Adv. Funct. Mater.* **29** 1807569
[9] Schouten M, Sanders R and Krijnen G 2017 *IEEE Sensors Conf.* (https://doi.org/10.1109/ICSENS.2017.8233949)
[10] Yao S and Zhu Y 2014 *Nanoscale* **6** 2345–52w
[11] Woo S-J, Kong J-H, Kim D-G and Kim J-M 2014 *J. Mater. Chem.* C **2** 4415–22
[12] Yang W *et al* 2018 *Adv. Mater. Technol.* **3** 1700241
[13] Vuorinen T, Laurila M-M and Mangayil R 2018 *IFMBE Proc.* **65** 839–42
[14] Guerin S *et al* 2018 *Nat. Mater.* **17** 180–6
[15] Sekine T, Sugano R, Tashiro T, Sato J, Takeda Y, Matsui H, Kumaki D, Domingues Dos Santos F, Miyabo A and Tokito S 2018 *Sci. Rep.* **8** 442
[16] Sekine T, Gaitis A and Sato J 2019 *ACS Appl. Electron. Mater.* **1** 246–52
[17] Laurila M-M, Peltokangas M, Lozano Montero K, Siponkoski T, Juuti J, Tuukkanen S, Oksala N, Vehkaoja A and Mantysalo M 2019 *IEEE Sens. J.* **23** 11072–80
[18] Sultana A, Ghosh S K, Sencadas V, Zheng T, Higgins M J, Middya T R and Mandal D 2017 *J. Mater. Chem.* **5** 7352
[19] Ghosh S K, Adhikary P, Jana S, Biswas A, Sencadas V, Gupta S D, Tudu B and Mandal D 2017 *Nano Energy* **36** 166–75
[20] Huang Y, Ding Y, Bian J, Su Y, Zhou J, Duan Y and Yin Z 2017 *Nano Energy* **40** 432–9
[21] Fuh Y K, Wang B S and Tsai C-Y 2017 *Sci. Rep.* **7** 6759
[22] Ma S, Ye T and Zhang T 2018 *Adv. Mater. Technol.* **3** 1800033
[23] Du Y, Wang R, Zeng M, Xu S, Saeidi-Javash M, Wu W and Zhang Y 2021 *Nano Energy* **90** 106522
[24] Yuan X, Gao X, Shen X, Yang J, Li Z and Dong S 2021 *Nano Energy* **85** 105985
[25] Wang Z L 2013 *ACS Nano* **11** 9533–57
[26] Cao R *et al* 2018 *Nano Res.* **7** 3771–9
[27] Wen D-L, Liu X, Deng H-T, Sun D-H, Qian H-Y, Brugger J and Zhang X-S 2019 *Nano Energy* **66** 104123
[28] Chen S *et al* 2018 *Adv. Funct. Mater.* **28** 1805108
[29] Zhu P, Zhang B, Wang H, Wu Y, Cao H, He L, Li C, Luo X, Li X and Mao Y 2022 *Nano Res.* **15** 7460–7
[30] Yi Q, Pei X, Das P, Qin H, Lee S W and Esfandyarpour R 2022 *Nano Energy* **101** 107511
[31] Lei H, Xiao J, Chen Y, Jiang J, Xu R, Wen Z, Dong B and Sun X 2022 *Nano Energy* **91** 106670
[32] Guo S-Z, Qiu K, Meng F, Park S H and McAlpine M C 2017 *Adv. Mater.* **29** 1701218
[33] Van Boven R W and Johnson K O 1994 *Neurology* **44** 2361
[34] Kim K, Choi J, Jeong Y, Cho I, Kim M, Kim S, Oh Y and Park I 2019 *Adv. Healthcare Mater.* **8** 1900978
[35] Abshirini M, Saha M, Altan M and Liu Y 2022 *Adv. Mater. Technol.* **7** 2101555
[36] Yin X-Y, Zhang Y, Cai X, Guo Q, Yang J and Wang Z L 2019 *Mater. Horiz.* **6** 767–80
[37] Li Q, Zhang L-N, Tao X-M and Ding X 2017 *Adv. Healthcare Mater.* **6** 1601371
[38] Honda W, Harada S, Arie T, Akita S and Takei K 2014 *Adv. Funct. Mater.* **24** 3299–304
[39] Yamamoto Y, Harada S, Yamamoto D, Honda W, Arie T, Akita S and Takei K 2016 *Sci. Adv.* **2** 1601473
[40] Nakata S, Arie T, Akita S and Takei K 2017 *ACS Sens.* **2** 443–8
[41] Vuorinen T, Niittynen J, Kankkunen T, Kraft T M and Mäntysalo M 2016 *Sci. Rep.* **6** 35289
[42] Wang Y-F, Sekine T, Takeda Y, Yokosawa K, Matsui H, Kumaki D, Shiba T, Nishikawa T and Tokito S 2020 *Sci. Rep.* **10** 2467
[43] Wang Z, Gao W, Zhang Q, Zheng K, Xu J, Xu W, Shang E, Jiang J, Zhang J and Liu Y 2019 *ACS Appl. Mater. Interfaces* **11** 1344–52
[44] Ali S, Khan S and Bermak A 2019 *IEEE Access* **7** 2949335
[45] Lei Z, Wang Q, Sun S, Zhu W and Wu P 2017 *Mater. Horiz.* **4** 694–700
[46] Wang Y, Qiu Y, Ameri S K, Jang H, Dai Z, Huang Y and Lu N 2018 *Npj Flex. Electron.* **2** 6
[47] Ameri S K, Ho R, Jang H, Tao L, Wang Y, Wang L, Schnyer D M, Akinwande D and Lu N 2017 *ACS Nano* **11** 7634–41
[48] Alberto J, Leal C, Fernandes C, Lopes P A, Paisana H, de Almeida A T and Tavakoli M 2020 *Sci. Rep.* **10** 5539
[49] Laurila M-M, Peltokangas M, Lozano Montero K, Verho J, Haapala M, Oksala N, Vehkaoja A and Mäntysalo M 2022 *Nano Energy* **102** 107625
[50] Lozano Montero K, Laurila M-M, Peltokangas M, Haapala M, Verho J, Oksala N, Vehkaoja A and Mäntysalo M 2021 *ACS Appl. Electron. Mater.* **3** 4362–75
[51] Khan S, Lorenzelli L and Dahiya R S 2015 *IEEE Sens. J.* **6** 3164–85
[52] Soltman D and Subramanian V 2008 *Langmuir* **5** 2224–31
[53] Laurila M-M, Matsui M and Shiwaku R 2019 *J. Electron. Device Soc.* **7** 566–74
[54] Choi C-H, Lin L-Y, Cheng C-C and Chang C-H 2015 *ECS J. Solid State Sci. Technol.* **4** P3044
[55] Kim C, Nogi M, Suganuma K and Yamato Y 2012 *ACS Appl. Mater. Interfaces* **4** 2168–73
[56] Shiwaku R *et al* 2018 *Sci. Rep.* **8** 3922
[57] Lozano Montero K, Laurila M-M and Mäntysalo M 2020 *IEEE 8th Electronics System-Integration Technology Conf. ESTC* (https://doi.org/10.1109/ESTC48849.2020.9229777)
[58] Sondergaard R R, Hösel M and Krebs F C 2012 *J. Polym. Sci.* B **1** 16–24
[59] Sondergaard R R, Hösel M, Angmo D, Larsen-Olsen T T and Krebs F C 2012 *Mater. Today* **1–2** 36–49
[60] Metters J P, Kadara R O and Banks C E 2011 *Analyst* **136** 1067–76
[61] Salmerón J F, Molina-Lopez F, Briand D, Ruan J J, Rivadeneyra A, Carvajal M A, Capitán-Vallvey L F, de Rooij N F and Palma A J 2014 *J. Electron. Mater.* **43** 604–17
[62] Zhang H *et al* 2015 *Adv. Mater.* **27** 201502639
[63] Grau G and Subramanian V 2016 *Adv. Electron. Mater.* **2** 1500328
[64] Minseok K, You I-K and Han H 2011 *Electrochem. Solid State Lett.* **8** 3591435
[65] Takeda Y, Sekine T and Wang Y-F 2020 *ACS Appl. Electron. Mater.* **3** 763–8
[66] Cho Y T, Jeong Y and Kim Y J 2017 *Appl. Sci.* **12** 1302
[67] Wiklund J, Karakoc A, Palko T, Yiğitler H, Ruttik K, Jäntti R and Paltakari J 2021 *J. Manuf. Mater. Process.* **5** 89
[68] Vallbo A B and Johansson R S 1984 *Hum. Neurobiol.* **3** 3–14
[69] Dagdeviren C *et al* 2015 *Nat. Mater.* **14** 728–36
[70] Webb R C *et al* 2013 *Nat. Mater.* **12** 938–44
[71] Ilves M, Lylykangas J, Rantanen V, Mäkelä E, Vehkaoja A, Verho J, Lekkala J, Rautiainen M and Surakka V 2019 *Biomed. Signal Process. Control* **48** 248–54
[72] Park K-I *et al* 2014 *Adv. Mater.* **26** 2514–20
[73] Kim S-Y *et al* 2016 *Nanoscale* **8** 17113–21
[74] Onses M S, Sutanto E, Ferreira P M, Alleyne A G and Rogers J A 2015 *Small* **34** 4237–66
[75] Park J-U *et al* 2007 *Nat. Mater.* **6** 782–9
[76] An B W, Kim K, Lee H, Kim S-Y, Shim Y, Lee D-Y, Song J Y and Park J-U 2015 *Adv. Mater.* **29** 4322–8
[77] Laurila M-M, Khorramdel B, Dastpak A and Mäntysalo M 2017 *J. Micromech. Microeng.* **9** 095005
[78] Laurila M-M, Khorramdel B and Mäntysalo M 2017 *IEEE Trans. Electron Devices* **3** 1217–24
[79] Laurila M-M, Soltani A and Mäntysalo M 2015 *IEEE 65th Electronic Components and Technology Conf. ECTC* (https://doi.org/10.1109/ECTC.2015.7159712)
[80] Yudistira H T, Nguyen V D, Dutta P and Byun D 2010 *Appl. Phys. Lett.* **96** 023503
[81] Optomec Aerosol jet technology (available at: www.optomec.com/printed-electronics/aerosol-jet-technology/) (Accessed 23 February 2023)

[82] Wilkinson N J, Smith M A A, Kay R and Harris R A 2019 *Int. J. Adv. Manuf. Technol.* **105** 4599–619
[83] Guo L J 2007 *Adv. Mater.* **4** 495–513
[84] Schäffner P, Zirkl M, Schider G, Groten J, Belegratis M R, Knoll P and Stadlober B 2020 *Smart Mater. Struct.* **8** 085040
[85] Moore G 1975 Progress in digital integrated electronics *Technical Digest Int. Electron Devices Meeting* (IEEE) pp 11–13
[86] Lewis J and Ahn B Y 2015 *Nature* **518** 42–3
[87] Macdonald E, Salas R, Espalin D, Perez M, Aguilera E, Muse D and Wicker R B 2014 *IEEE Access* **2** 234–42
[88] Lee J, Kim H-C, Choi J-W and Lee I H 2017 *Int. J. Precis. Eng. Manuf.-Green Technol.* **4** 373–83
[89] Lewis J 2006 *Adv. Funct. Mater.* **16** 2193–204
[90] Viscotec 3D printing (available at: www.viscotec.de/en/industry-applications/3d-printing/) (Accessed 23 February 2023)
[91] Jordan R S and Wang Y 2019 *J. Polym. Sci.* **57** 1592–605
[92] Reneker D H and Chun I 1996 *Nanotechnology* **7** 216
[93] Subbiah T, Bhat G S, Tock R W, Parameswaran S and Ramkumar S S 2005 *J. Appl. Polym. Sci.* **2** 557–69
[94] Tobjörk D and Österbacka R 2011 *Adv. Mater.* **23** 1935–61
[95] Yoshida M, Onogi T, Onishi K, Inagaki T and Tajitsu Y 2014 *Jpn. J. Appl. Phys.* **53** 09PC02
[96] Rajala S, Siponkoski T, Sarlin E, Mettanen M, Vuoriluoto M, Pammo A, Juuti J, Rojas O J, Franssila S and Tuukkanen S 2016 *ACS Appl. Mater. Interfaces* **24** 15607–14
[97] Hänninen A, Sarlin E, Lyyra I, Salpavaara T, Kellomäki M and Tuukkanen S 2018 *Carbohydr. Polym.* **15** 418–24
[98] Basavalingappa V 2020 *ACS Nano* **6** 7025–37
[99] Trung T Q and Lee N-E 2016 *Adv. Mater.* **22** 4338–72
[100] Ray T R, Choi J, Bandodkar A J, Krishnan S, Gutruf P, Tian L, Ghaffari R and Rogers J A 2019 *Chem. Rev.* **8** 5461–533
[101] Jankovic J, Schwartz K S and Ondo W 1999 *J. Neurosurg. Psychiatry* **67** 646–50
[102] Kaindlstorfer C, Granata R and Wenning G K 2013 *Tremor and Other Hyperkinetic Movements* **3** 3779823
[103] Yang J K, Ahn N E, Kim D H and Kim D Y 2014 *Ann. Rehabil. Med.* **2** 145–52
[104] Bacarin T A, Sacco I C N and Hennig E M 2009 *Clinics* **2** 113–20
[105] Son D *et al* 2014 *Nat. Nanotechnol.* **9** 397–404
[106] Wu Y, Liu Y and Zhou Y 2018 *Sci. Robot.* **22** 0429
[107] O'Rourke M F and Hashimoto J 2007 *J. Am. Coll. Cardiol.* **1** 1–13
[108] O'Rourke M F and Gallagher D E 1996 *J. Hypertens.* **5** 147–57
[109] Haapala M, Lyytikäinen L-P and Peltokangas M 2021 *Atherosclerosis* **319** 101–7
[110] World Health Organization 2018 *Assessing national capacity for the prevention and control of noncommunicable diseases: report of the 2017 global survey* (World Health Organization)
[111] Strollo P J and Rogers R M 1996 *New Engl. J. Med.* **334** 99–104
[112] Chorsi M T, Curry E J and Chorsi H T 2019 *Adv. Sci. News* **31** 1802084
[113] Kamalasanan M N, Chandra S, Joshi P C and Mansingh A 1991 *Appl. Phys. Lett.* **59** 3547
[114] Nair K M, Bhalla A S and Hirano S-I 2003 *Ceramic Materials and Multilayer Electronic Devices* (New York: Wiley)
[115] Jiang X, Tang F, Wang J T and Chen T-P 2001 *Physica* C **364** 678–83
[116] Sessler G M 1981 *J. Acoust. Soc. Am.* **70** 1596
[117] Piezotech FC datasheet (available at: www.piezotech.eu/en/Technical-center/Documentation/) (Accessed 23 February 2023)
[118] Pan Q Y, Tasaka S and Inagaki N 1996 *Jpn. J. Appl. Phys.* **35** 1442
[119] Wang X-Y, Lee C-Y, Peng C-J, Chen P-Y and Chang P-Z 2008 *Sens. Actuators* A **143** 469–74
[120] Hu J, Duan W, Fan S and Xiao H 2022 *Measurement* **190** 110724
[121] Siponkoski T, Nelo M, Palosaari J, Peräntie J, Sobocinski M, Juuti J and Jantunen H 2015 *Composites* B **80** 217–22
[122] Alamusi A 2012 *Nanoscale* **4** 7250
[123] Achaby M E, Arrakhiz F Z, Vaudreuil S, Essassi E M and Qaiss A 2012 *Appl. Surf. Sci.* **258** 7668–77
[124] Wang S, Lin L and Wang Z L 2015 *Nano Energy* **11** 436–62
[125] Wang Z L, Lin L and Chen J 2016 *Triboelectric Nanogenerators* (Berlin: Springer)
[126] Yang Y, Chen L, He J, Hou X, Qiao X, Xiong J and Chou X 2021 *Adv. Mater. Technol.* **7** 2100702
[127] Ma L, Xia T, Yu R, Lei X, Yuan J, Li X, Cheng G J and Liu F 2021 *Adv. Eng. Mater.* **23** 2100379
[128] Stassi S, Cauda V, Canavese G and Pirri C 2014 *Sensors* **14** 5296–332
[129] Sharma S, Chhetry A and Sharifuzzaman M 2020 *ACS Appl. Mater. Interfaces* **12** 22212–24
[130] Diridollou S, Vabre V and Berson M 2001 *Int. J. Cosmet. Sci.* **23** 353–62
[131] Elsner P, Barel A O and Lambrecht R 1998 *Skin Bioengineering Techniques and Applications in Dermatology and Cosmetology* (Basel: Karger Medical and Scientific Publishers) pp 69–83
[132] Kurz A 2008 *Best Pract. Res. Clin. Anaesthesiol.* **4** 627–44
[133] Murphy P J and Campbell S S 1997 *Sleep* **7** 505–11
[134] Czeisler C A, Zimmerman J C and Ronda J M 1980 *Sleep* **3** 329–46
[135] Lahiri B B, Bagavathiappan S, Jayakumaret T and Philip J 2012 *Infrared Phys. Technol.* **55** 221–35
[136] Kennedy D A, Lee T and Seely D 2009 *Integr. Cancer Ther.* **1** 9–16
[137] Sivanandam S, Anburajan M, Venkatraman B, Menaka M and Sharath D 2012 *Endocrine* **42** 343–51
[138] Katerinopoulou D, Zalar P, Sweelssen J, Kiriakidis G, Rentrop C, Groen P, Gelinck G H, van den Brand J and Smits E C P 2019 *Adv. Electron. Mater.* **5** 1800605
[139] Dinh T, Phan H-P, Qamar A, Woodfield P, Nguyen N-T and Dao D V 2017 *J. Microelectromech. Syst.* **5** 966–86
[140] Miyamoto A *et al* 2017 *Nat Nanotechnol* **12** 907–13
[141] Zhu P, Wang Y, Wang Y, Mao H, Zhang Q and Deng Y 2020 *Adv. Energy Mater.* **5** 2001945